Effect of Formation Heterogeneity on CO₂ Dissolution in Subsurface Porous Media

Md Fahim Shahriar¹, Aaditya Khanal^{1*}

¹The Jasper Department of Chemical Engineering, The University of Texas at Tyler, Tyler, TX 75799, United States Corresponding author E-mail address: aadityakhanal@uttyler.edu

5 6 7

4

1 2 3

To Cite: Shahriar, M. F., & Khanal, A. (2023). Effect of Formation Heterogeneity on CO 2 Dissolution in Subsurface Porous Media. ACS Earth and Space Chemistry. https://doi.org/10.1021/acsearthspacechem.3c00175

8 9 10

11

12

13 14

15

16

17

18

19

20

21

22

23

24

25

26

27 28

29

30

31

32

33

34

35

3637

38

39

40

41

42

43

44

45

46

47

48

49

50

51

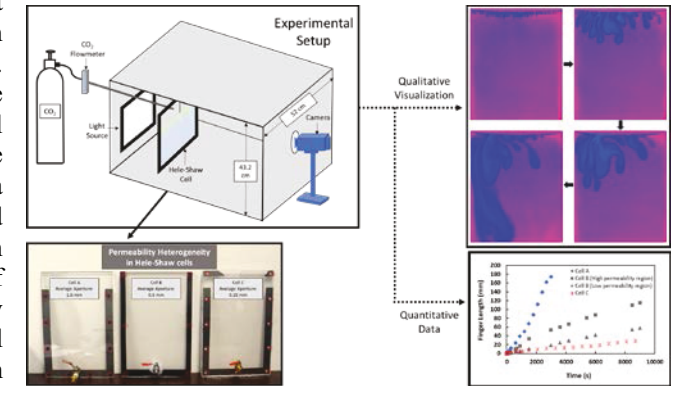
52

53

54

Abstract

Dissolution trapping is one of the most dominant mechanisms for secure storage of CO₂ injected in porous subsurface formations saturaFted with brine. This trapping mechanism is enhanced by convective mixing, which occurs due to the gravitational instability between the different fluid layers in the aquifer. The reservoir permeability also plays a crucial role in the dissolution rate and overall fluid flow dynamics during the density-driven convection in porous media. This study investigates the role of complex heterogeneity, i.e., irregular permeability distribution in CO2 dissolution, using a novel approach experimental to create medium permeability heterogeneity in Hele-Shaw cells.



Complex subsurface transport phenomena such as preferential dissolution path, CO_2 sweep efficiency, changes in finger morphology, and CO_2 concentration distribution are visualized by creating heterogeneous media. Experimental results showed reservoir permeability heterogeneity causes significant channeling effects and poor sweep efficiency. A scaling relationship between average finger growth rate (Gr) and permeability (k) was obtained as Gr [m. s^{-1}] = 266.8k [m²] + 1.20×10^{-6} . Furthermore, the mass of CO_2 dissolved is calculated using the spectrophotometric method to characterize the convective instability. The convective flux was analyzed by comparing experimental dissolution flux with theoretical diffusion flux, calculating a maximum Sherwood number of 6.8. The study's findings improve the current understanding of the CO_2 convection morphology in heterogeneous media, allowing better assessment of long-term CO_2 storage.

Keywords: CO₂ Sequestration; Spectrophotometric Method; Preferential Flow; Hele-Shaw cell; Heterogeneity; Permeability Contrast

1. Introduction

The atmospheric concentration of CO₂, which was recorded as 424 parts per million (ppm) in June 2023 [1], has increased by approximately 50% compared to the beginning of the industrial revolution [2]. Further increases in atmospheric CO₂ levels may raise the global temperature over 1.5°C above the pre-industrial level, which may cause irreversible damage to vital ecosystems across the globe. The effect of rising surface temperatures due to increased atmospheric CO2 is evident from numerous and frequent natural disasters, resulting in massive economic losses estimated to exceed \$2.275 trillion [3] from 1980 alone. Consequently, there is a growing interest in reducing the concentration of atmospheric CO₂ by switching to renewable/low-emission energy sources and reducing CO₂ emissions by other means [4–6]. Geological sequestration of CO₂ is one the most promising technologies that can safely sequester carbon emissions from large stationary sources and slow the harmful increase of CO₂ concentrations in the atmosphere [7,8]. Among the subsurface storage options, deep saline aquifers are one of the major geological storage options because of their wide availability and huge storage potential [5]. CO₂ is stored in deep saline aquifers by four primary trapping mechanisms: structural, residual, dissolution, and mineral trapping. Even though residual trapping is dominant at the early stages of CO₂ storage, dissolution trapping becomes the primary trapping mechanism with time, capturing almost two-thirds of CO₂ injected in the storage volume [9–11]. The precursor for dissolution trapping is a slow process of molecular diffusion. However, the dissolution rate increases subsequently by other mechanisms such as density-driven convection or Rayleigh-Taylor instability, dispersion, and advection [12,13]. Several factors can affect the convective-dissolution phenomenon for different geological sites and, therefore, need to

be considered for accurate CO₂ storage prediction. Density-driven convection is significant in safe CO₂ storage, as it

promotes quick CO₂ sinking rather than rising to shallower formations [9]. The positive effect of density-driven convection has led to various studies about characterizing the transport mechanisms and the effect of different parameters during density-driven convection or Rayleigh-Taylor instability [14–20].

55 56

57

58

59

60

61

62 63

64

65

66

67 68

69

70

71

72

73

74

75

76

77

78

79

80

81

82

83

84 85

86

87

88

89

90

91

92

93

94

95

96

97

98

99

100

101

102

103 104

105

106 107

108

109

The Hele-Shaw cell, a simple apparatus built with a small aperture between two transparent flat plates, has been extensively used to visualize the Darcy flow, including the density-driven CO₂ transport. Furthermore, by varying several parameters in the cell, such as aperture, porosity, and vertical or horizontal permeability, it is possible to mimic the transport mechanism similar to that of CO₂ storage in different geological structures [21-26]. These experimental studies have adopted different visualization techniques to investigate the finger morphology during density-driven CO₂ transport, such as the pH indicator-based method, Schlieren method, particle image velocimetry (PIV), laserinduced fluorescence (LIF), and interferometry method [9,20,27–29]. Furthermore, several studies have investigated scaling relationships to characterize the convective dissolution rate of CO₂ in brine formations [29–33]. Motjaba et al. [30] developed a relationship between Sherwood and Rayleigh numbers and CO₂ convective flux at different Rayleigh numbers under 3.45 MPa and 182 < Ra <20860. Mahmoodpour et al. [34] showed scaling relationships between compensated flux and transition times between successive regimes in the system for experimental fluid with different salt types (NaCl and CaCl₂). Faisal et al. [31] obtained correlations between dissolved CO₂ mass and different Rayleigh numbers. Different theoretical studies on the onset of convection and the initial convective instability wavelength were also discussed and identified [10,35,36]. Several studies also investigated CO₂ dissolution at high pressure and high temperature (HPHT) conditions, mimicking the actual reservoirs. Outeda et al. [21] investigated how a change in pressure (1.5-5 bar) affects the CO₂ dissolution phenomenon. All the experiments were conducted at a constant temperature of 25 °C. Higher pressure was observed to increase CO₂ mass influx to the aqueous phase, thus promoting faster CO₂ storage. Furthermore, higher pressure also caused an early initiation of convective instability. At the lowest pressure of 1.5 bar, the instabilities were observable at around 60 s, whereas the instabilities could be seen as early as 10 s for 5 bar. Mahmoodpour et al. [34] investigated the dissolution-driven convection at high-pressure conditions (up to 535.3 psi), while Tang et al. [9] observed the convection parameters, including critical onset time of convection, dissolution rate, and gravitational instabilities in a Hele-Shaw cell rated to 70 MPa and Ra of 346. The studies show that CO₂ sequestration is preferable under HPHT conditions. It is also worth noting that no significant change in CO₂ finger morphology was reported due to pressure or temperature variation, thereby making it safe to assume that the fundamental qualitative findings in this study can be translated to HPHT conditions.

Several studies have employed various methods to calculate the mass of dissolved CO₂ in laboratory dissolution experiments. By calculating the changes in situ CO₂ gas phase from the gas tank and the empty parts of the Hele-Shaw cell, Taheri et al.[37] measured the dissolved CO₂ in each step. Faisal et al. [31] measured the total dissolved CO₂ mass by analyzing the carbon content in the experimental fluid using a TOC-L analyzer. Mojtaba et al. [30] examined the CO₂ dissolution rate by recording the pressure decay data during CO₂ dissolution. Guo et al. [38] established an empirical linear correlation between the solute (methanol-ethylene-glycol) concentration and reflected light intensity, using which they calculated dissolved mass flux. A novel spectrophotometric method was developed in the works of Teng et al. [39,40]. The technique used the gray value of each experimental image and obtained the corresponding CO₂ concentration using correlations between absorbance and concentration of attenuating species.

Heterogeneity, a characteristic feature of natural porous media, can strongly influence the spatial permeability distribution, thus governing the dispersion behavior of the density-driven flow of CO₂-rich fluid [41–44]. Subsurface heterogeneities can be of different scales and forms, including petrophysical heterogeneity (hydrofacies transition), biological heterogeneity (growth of biofilm), chemical heterogeneity (mineralogical change), and others [41,42]. Among these, petrophysical-based heterogeneities (e.g., variability in permeability and porosity) can significantly impact the CO₂ flow morphology, thus necessitating prior knowledge of spatial heterogeneities' effect on CO₂ dissolution for selecting storage sites [45–47]. The reservoir heterogeneities may arise from structural heterogeneities due to the presence of faults, salt diapers or folds, and the presence of heterogeneous stratigraphic facies [48,49], and all the CO₂ subsurface storage sites have some flow space heterogeneity at all geologic scales from pore [50] to reservoir scales [51,52]. Shahriar and Khanal [20] observed preferential finger movement and channeling effect by introducing heterogeneity in Hele-Shaw cells. Amarasinghe et al. [53] investigated CO₂ dissolution using 400-600 µm glass beads in a porous media. Similar glass bead sizes were also adopted in the work of Vosper et al. [54] at different temperatures and pressures. Soltanian et al. [45] performed a high-resolution simulation to investigate CO₂ dissolution trapping in heterogeneous formations, where facies spatial organization was observed affecting CO2 convective mixing dynamics. Wang et al. [55] reported the gas channeling effect, i.e., accelerated CO₂ migration along high permeability regions in numerically modeled heterogeneous reservoirs. Furthermore, residual oil zones with a high degree of heterogeneity were concluded to have deteriorated CO₂ sequestration efficiency. Despite the considerable investigative analyses on CO₂ dissolution-driven convection in a heterogeneous medium using the Hele-Shaw cell,

most experimental studies, to our knowledge, focus on introducing heterogeneity by using strips or sand beads to create a non-uniform aperture, thus presenting simple heterogeneity, i.e., stacking varying permeability regions vertically or horizontally [14,17,20]. Although these experimental studies contribute to knowledge of flow nature in heterogeneous media, they present a layered heterogeneity approach and do not mimic the irregular permeability heterogeneity in actual reservoirs. Thus, further experimental studies on CO₂ dissolution in complex heterogeneous media are required [51,56]. Furthermore, although some numerical simulations have focused on the effect of spatial permeability variation, experimental studies are needed to gain physical knowledge to validate and improve the modeling works [45,55].

This experimental study focuses on CO₂ convection dynamics on complex heterogeneous media, thereby investigating preferential flow path, irregular finger movement, and other subsurface CO2-storage phenomena. Furthermore, based on the literature surveyed, only three studies have used the spectrophotometric method to quantify the mass of CO₂ dissolved during the experiment [18,39,40]. Compared to using an organic carbon analyzer, which calculates the mass of CO₂ dissolved only at the end of the experiment [31], the spectrophotometric method enables real-time quantitative characterization of CO₂ dissolution without needing a complex experimental setup [40]. Previous studies calculated cumulative dissolved CO₂ concentration with spectrophotometric analysis using gray values of the experimental images [18,39,40]. However, to expand existing knowledge on this method, this study uses a modified spectrophotometric method, using three different color channels- red, blue, and green values, and selects the color channel with the highest correlation with calculating dissolved CO₂. The novelty of this work is to (1) experimentally investigate the CO₂ transport under stochastically generated variable spatial heterogeneity conditions and (2) introduce a modification in the spectrophotometric method for quantitative characterization of CO₂ dissolution. The remainder of the paper is organized as follows. Section 2 provides the governing equations and dimensionless parameters used in this study. Section 3 presents the experimental methods and image processing sequence. Section 4 presents the theory of generating permeability maps and the procedure of setting up medium permeability heterogeneity. Section 5 reports the qualitative visualization of CO₂ dissolution in heterogeneous media for different average permeability regions. Section 6 presents our findings regarding the quantitative characterization of CO₂ dissolution. Lastly, Section 7 presents the summary and main conclusion of this study.

2. Governing Equations and Dimensionless Parameters

2.1. Governing Equations

The governing conservation equation explaining the density-driven CO₂ transport in equilibrium conditions considers formation brine (existing in the aqueous (*l*) phase) and CO₂ gas (existing in the gaseous (*g*) phase) overlaying on top of the brine and is formulated as [31].

$$\frac{\partial}{\partial t} \left[\sum_{\gamma = l, g} \left(\Phi \rho_{\gamma} S_{\gamma} \omega_{\gamma}^{i} \right) \right] = - \sum_{\gamma = l, g} \nabla \left(\rho_{\gamma} \mathbf{V}_{\gamma} \omega_{\gamma}^{i} \right) - \sum_{\gamma = l, g} \nabla \left(\mathbf{J}_{\gamma}^{i} \right) + \sum_{\gamma = l, g} \left(m_{d\gamma} \omega_{\gamma}^{i} \right)$$

$$\tag{1}$$

Where γ represents the gaseous or liquid phase, i represents CO_2 or H_2O , Φ is porosity, ρ is density (kg/m³), S represents saturation, ω is the mass fraction, m_d represents the mass rate density. The governing equations dictating convective mixing consist of the convective diffusion equation for transporting dissolved CO_2 and Darcy's law for fluid motion [57]. Furthermore, the Boussinesq assumption is considered in the conservation of mass, momentum, and species, stating that solute concentrations cause local density change without any expansion or contraction of the experimental fluid [58].

 V_{γ} represents the advective fluxes (m/s), computed using Darcy's law for gaseous and liquid phases as expressed below [31,59].

$$V_{\gamma} = -\frac{k_{r\gamma}d_{avg}^{2}}{\mu_{\gamma} \times 12} (\nabla P_{\gamma} + \rho_{\gamma}g\mathbf{z})$$
 (2)

Where d_{avg} is the average Hele-Shaw cell aperture, k_r is relative permeability, P is pressure (Pa), g is gravitational acceleration (m/s²), μ (Pa s) is dynamic viscosity, and z is unit gravitation direction vector. The term $(d_{avg}^2/12)$ refers to the cell's intrinsic permeability (k). To account for spatial permeability variation due to aperture change, the average cell aperture (d_{avg}), calculated following the method of Detwiler et al. [60] and Faisal et al. [31], is used for intrinsic permeability calculation. By considering the molecular diffusion, diffusive fluxes J (kg/m³s) are calculated which can be expressed as

$$J_{\gamma}^{i} = -\Phi \rho_{\gamma} S_{\gamma} \frac{M^{i}}{M_{\nu}} (\tau_{\gamma} D_{\gamma}^{i}) \nabla X_{\gamma}^{i}$$
(3)

Where M is molecular weight (kg/kmol), τ is tortuosity, X is mole fraction, and D is diffusion coefficient (m²/s). Based on the Hele-Shaw cell analogy, uniform tortuosity is considered [31]. We suggest the report of White et al. [61] to readers interested in the detailed description of all the state equations.

2.2. Dimensionless Parameters

The CO₂ convective dissolution in this study was evaluated using characteristic dimensionless parameters relevant to CO₂ flow in deep saline aquifers. Rayleigh number (Ra), a dimensionless number characterizing the system by expressing the ratio of free convection to diffusion, can be represented, as shown in **Eq. 4**:

$$Ra = \frac{\Delta \rho g k H}{\mu \varphi D_{CO_2}} \tag{4}$$

Where g is the acceleration due to gravity $[m/s^2]$, H is the water column height [m], and μ is the dynamic viscosity of water [kg/m.s], D_{CO_2} is the molecular diffusion coefficient of CO_2 in water $[m^2/s]$, k is the permeability of the medium $[m^2]$, $\Delta \rho$ is the increase in density due to CO_2 dissolution $[kg/m^3]$, and φ is porosity. The fluid properties are collected from Faisal et al. [31], as the experiments are conducted at same atmospheric conditions. Based on theoretical studies, if the value of Ra is greater than a critical value equal to $4\pi^2$, natural convection is preponderant [31,62]. The experiments considered in this study are designed to meet this criterion. The permeability of a Hele-Shaw cell, k, with uniform cell aperture of b, can be obtained from the fundamental conservation laws as [63]:

$$k = \frac{b^2}{12} \tag{5}$$

Three different Hele-Shaw cells (average aperture of 1.6, 0.6, and 0.26 mm) are used in this study, where the aperture is significantly smaller than the height of the water column (198 mm).

A crucial dimensionless ratio used for characterizing the flow configuration is anisotropy ratio (ϵ), expressed as [23]:

$$\epsilon = \frac{b}{\sqrt{12}H} \tag{6}$$

The combined action of the anisotropy ratio and Rayleigh number, formulated as $\epsilon^2 Ra$, was developed to classify flow configurations into three types, where for (i) $\epsilon^2 Ra \to 0$, the flow is two-dimensional and mathematically analogous to Darcy flow; (ii) $\epsilon^2 Ra$ "0, the flow is still two-dimensional and is under the Hele-Shaw regime; however, gap-induced dispersion needs to be brought into consideration, and (iii) $\epsilon^2 Ra$ "1, the fluid flow is no longer 2D, and thus, the effects of the third dimension are non-negligible [23,64,65].

Table 1. Hele-Shaw cell permeability distribution and calculated properties

Cell Name	Average Aperture, b [mm]	Permeability Distribution	Raª	$\epsilon^2 R a^{\mathrm{b}}$	k [m²]ª
Cell A	1.6	Irregular distribution	86816	0.4724	$2.13 \times 10^{-7} \text{ m}^2$
Cell B	0.6	 Higher permeability at the sides (3 to 5 × 10⁻⁸ m² Lower permeability at the middle (2 to 3 × 10⁻⁸ m²) 	12279	0.0094	$3 \times 10^{-8} \text{ m}^2$
Cell C	0.26	Irregular distribution	2389	0.0003	$5.63 \times 10^{-9} \mathrm{m}^2$

^aValues Calculated using Average Aperture; ^bWater column height, H, is 198 mm for all the cells

As shown in Table 1, all the cells exhibit 2D fluid flow, and thus, the flow environment considered in this study is mathematically analogous to the Darcy flow in isotropic porous media [20,23]. However, the effect of gap-induced dispersion is not negligible in cell A and will be explained in detail in Section 4.

Sherwood number, Sh, is also used to characterize the mass flux in dimensionless form, expressed as the ratio of the convection mass flux to the diffusive flux [40], as shown in Eq. 7.

$$Sh = \frac{F_C}{\varphi \Delta c \, D_{CO_2}/H} \tag{7}$$

Where, $F_C = \varphi u \Delta c$ is the convective flux, Δc is the concentration difference between the liquids, and u is the characteristic velocity.

3. Experimental Methods and Procedures

3.1. Experimental Setup

As illustrated in **Fig. 1**, the basic experimental setup consists of the Hele-Shaw cell placed inside an isolated chamber with a uniform LED light source, thus preventing any background noise or external disturbance throughout the experiment. The experimental apparatus and relevant comments adopted in this study are explained in **Table 2**. The Hele-Shaw cell comprises two transparent 25.4-mm-thick plexiglasses separated by precision shims of graphite or silicone. Plexiglass is considered in this study as it provides enhanced clarity compared to glass [20]. The transparent plexiglass has a length and height of 203 mm and 304 mm, respectively. Experiments are performed on atmospheric conditions (22 °C and 1.01 bar), where the Hele-Shaw cell is filled with a solution prepared by mixing deionized, de-aired water with 0.0114% w/v Bromocresol Green (BCG) through a ball valve fitted at the bottom of the cell. This port was used to fill and drain the reactor of the experimental fluid. BCG is a pH indicator that changes color from blue at a pH above 5.4 to yellow at a pH of around 3.9 [62]. Furthermore, a hole is drilled at the center of the front plexiglass so that the CO₂ can be securely injected into the cell using an 18-gauge dispensing needle.

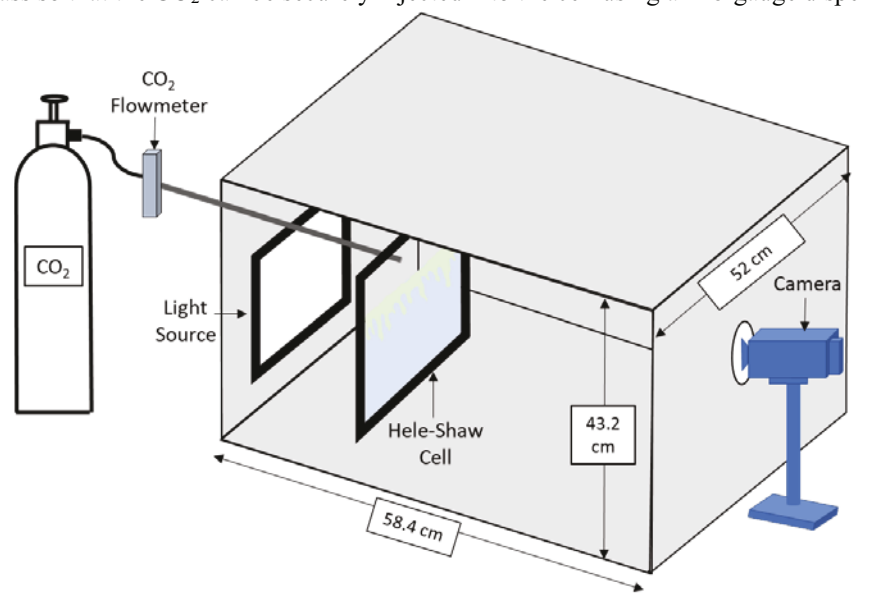


Fig. 1. Schematic of the experimental setup shows (from left to right): CO₂ cylinder, flowmeter, light source, and Hele-Shaw with experimental fluid inside an isolated chamber and a digital camera for continuous image capture of CO₂ dissolution.

Table 2. Additional comments regarding the experimental apparatus adopted in this study

Experimental Apparatus	Additional Comments
Hele-Shaw Cell	Three different Hele-Shaw cells (average aperture of 1.6, 0.6, and 0.26 mm) are used in this study. (Refer to Table 1 for a detailed description.)
CO ₂ Flowmeter (Dakota Instruments, 6A01 Acrylic Flow Meter)	It is crucial to inject CO ₂ at a small flow rate so that the water interface at the top of the cell is not disturbed, as such disturbance can influence the finger morphology in the cell [20,31]. Therefore, this study uses a flow rate of 0.59 L/min, continuously monitored by a flowmeter, which showed no impact on the fluid interface.

Light Source (LitEnergy	The light tracing box fitted with flicker-free LED lamps, powered by DC, with
A4 LED Copy Board Light	adjustable brightness levels, was used as the only light source. A maximum
Tracing Box)	illuminance of 100 lux was selected as the incident light source for all the
	experiments considered in this study.
Camera (Nikon D7000 with	The CO ₂ dissolution region experiences significant changes in shape during the
50 mm lens, maximum	initial experimental stage, i.e., until the qualitative onset time of convection
resolution: 4928 × 3264)	[20,31,37,62]. To accurately capture the initial changes in the flow regime, images
	were collected at 1-second intervals for the first 15 minutes and at 5-second intervals
	for the remainder of the experiment.

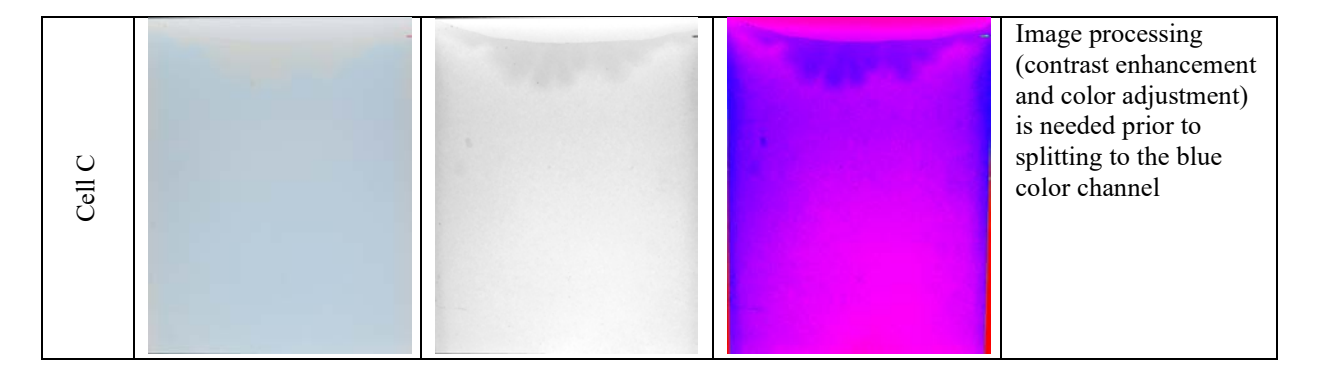
A small hole is created on the back of the isolated chamber to place the CO₂ inlet pipe in the Hele-Shaw cell. Another hole is made in the front of the isolated chamber to capture images of convective dissolution in the flow cell with a Nikon D7000 digital camera with a 50 mm lens. The experiments are continued until the CO₂-dissolved region reaches the bottom of the cell, or up to 2.5 hours, whichever is shorter.

3.2. Image Capture and Enhancement Methodology

By placing the Hele-Shaw cell inside the isolated chamber and using a uniform LED board as the only light source, background disturbance or external reflections are eliminated. Although the CO₂ fingers are observable with the naked eye, it is challenging to notice the minute details of concentration change in the finger morphology with the raw images. Although previous studies applied image processing for better visualization, most techniques do not highlight the subtle CO₂ concentration differences inside the cell based on color scale level [37,40,62]. Therefore, this study adopts a color scale-based image-processing technique to visualize the concentration difference inside the CO₂-dissolved region.

Table 3. Image Processing sequence for the Hele-Shaw cells considered in this study

Cell Considered	Raw Image	Blue Color Channel	Final Image	Additional Comments
Cell A		Se de la constitución de la cons		No image adjustment is needed prior to splitting to the blue color channel
Cell B				Image processing (contrast enhancement and color adjustment) is needed prior to splitting to the blue color channel



The image processing is performed using ImageJ FIJI, where any background noise is discarded prior to splitting the images into three color channels. We observed the blue channel to capture the finger morphology accurately, compared to the red and green channels (refer to Section 5.2 for more details). Therefore, the blue channel is used, and a spectrum-based lookup, based on a color scale of 0-255, is applied to the images, as shown in **Table 3**. As shown in **Table 3**, for cells B and C, with an average aperture of 0.6 mm and 0.26 mm, respectively, it is difficult to observe the color change in the raw images due to the lower volume of fluid occupying the cell region. Therefore, if needed, further image processing (contrast enhancement and color adjustment) is performed.

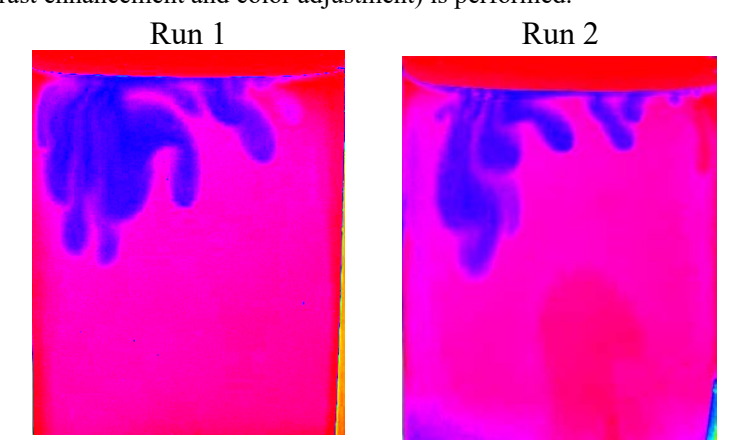


Fig. 2. Two visualization results for Cell A at 25 minutes showing good reproducibility in terms of similar overall convective pattern

Before conducting the experimental studies, repeatability is verified by visually comparing the finger patterns for two different runs in identical conditions, as presented in **Fig. 2**. As shown in **Fig. 2**, the two experiments exhibit similar finger morphology and vertical travel at the same timescale. Some minor dissimilarities are observed, which can be attributed to slight changes in the experimental setups as expected for experiments in Hele-Shaw cells in prior studies [20,31]. Nevertheless, similar CO₂ transport patterns observed in the two runs ensure the repeatability of the experiments.

4. Medium Heterogeneity in Hele-Shaw Cell

4.1. Permeability Field

Since permeability is proportional to the square of the cell aperture (**Eqn. 8**), a slight aperture variation will also correspond to different permeable regions, thereby affecting the flow behavior. The spatial distribution of flow cell aperture is measured by using the Beer-Lambert law [66], which relates the transmitted light intensity *I* through a light-absorbing solute as:

 $I = I_o e^{-\mu C d + \xi} \tag{8}$

where the incident light intensity is I_o , the absorptivity of the solute is μ , d is the aperture, solute concentration is C, and ξ is a constant accounting for solvent absorbance and the cell filled with solute [31,60]. Two different solute concentrations (C_I and C_2), with constant incident light intensity, can be expressed as:

$$\ln\left(\frac{l_1}{l_2}\right) = \mu(C_2 - C_1)d = A \tag{9}$$

where absorbance A of the solute is a linear function of concentration. The light intensity transmitted through a transparent fracture, I_{ij} (where i and j represent the location of each measurement within the Hele-Shaw cell), is collected. By assuming constant μ , C_{I_1} and C_{I_2} , where $C_{I_2} = 0$ and $C_{I_2} = 0$, and averaging over the entire cell yields:

$$\langle A_{ij} \rangle = \langle \ln \left(I_{cl} / I_{dye} \right) \rangle = \mu C \langle d_{ij} \rangle$$
 (10)

where, I_{cl} and I_{dye} represents intensities for C_1 and C_2 fields, respectively, and $\langle \rangle$ indicates spatial averaging over all the measurements. Combining Eq. (9) and (10) results in:

$$d_{normij} = d_{ij}/\langle d_{ij} \rangle = A_{ij}/\langle A_{ij} \rangle \tag{11}$$

Following the method of Detwiler et al. [60] and Faisal et al. [31], the average cell aperture (d_{avg}) is calculated by filling the cell with a known volume of fluid. Since the normalized light intensity varies proportionally with fluctuations in cell aperture, by combining the normalized light intensity data with average cell aperture, aperture variations throughout the cell can be calculated. Three different cells were considered in this study, as shown in **Table**

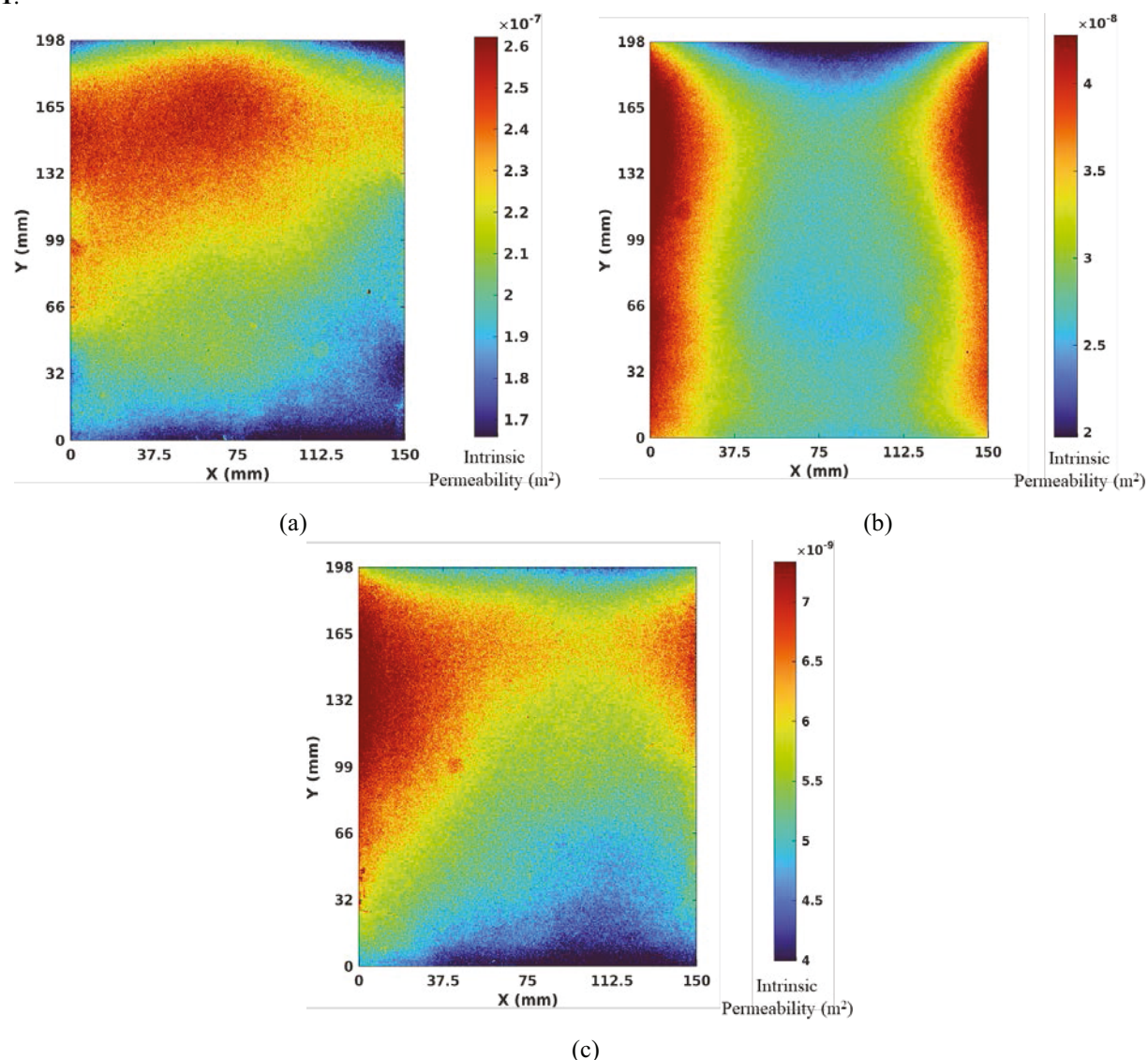


Fig. 3. Permeability maps resulting from the transmitted light analysis on the experimental Hele-Shaw cell configurations: (a) Cell A, (b) Cell B, and (c) Cell C

The variable light intensity data is transformed into an aperture field, and a corresponding permeability map is generated for the three Hele-Shaw cells, as shown in **Fig. 3**. While getting the permeability map from the light intensity data, the smudges or marks in the Hele-Shaw cell can generate inaccurate data points, resulting in extremely high or low permeability values for those points. Thus, the final permeability map is constrained by setting the limit as two standard deviations from the mean permeability to prevent outliers. The procedure of devising medium permeability is discussed in the following subsection.

4.2. Setting up Medium Heterogeneity

Different spatial permeability heterogeneity mediums are created by carefully varying the shim placement on the sidewalls of the Hele-Shaw cells, illustrated in Fig. 4. The graphite shims are placed and tightened up to the water column height in cell A, with a 1.6 mm average aperture. By doing so, a higher aperture is obtained at the top of the cell due to the presence of no tightening force, where the aperture varies throughout the cell in a parabolic manner, as evident in the permeability map of the 1.6 mm cell, shown in **Fig. 5**. However, since this study aimed to investigate the effect of complex permeability distribution, i.e., irregular permeability distribution, the right uppermost bolt was tightened slightly higher to get irregular permeability distribution, although some resemblance with a parabolic permeability profile remains, as shown in **Fig. 3** (a).

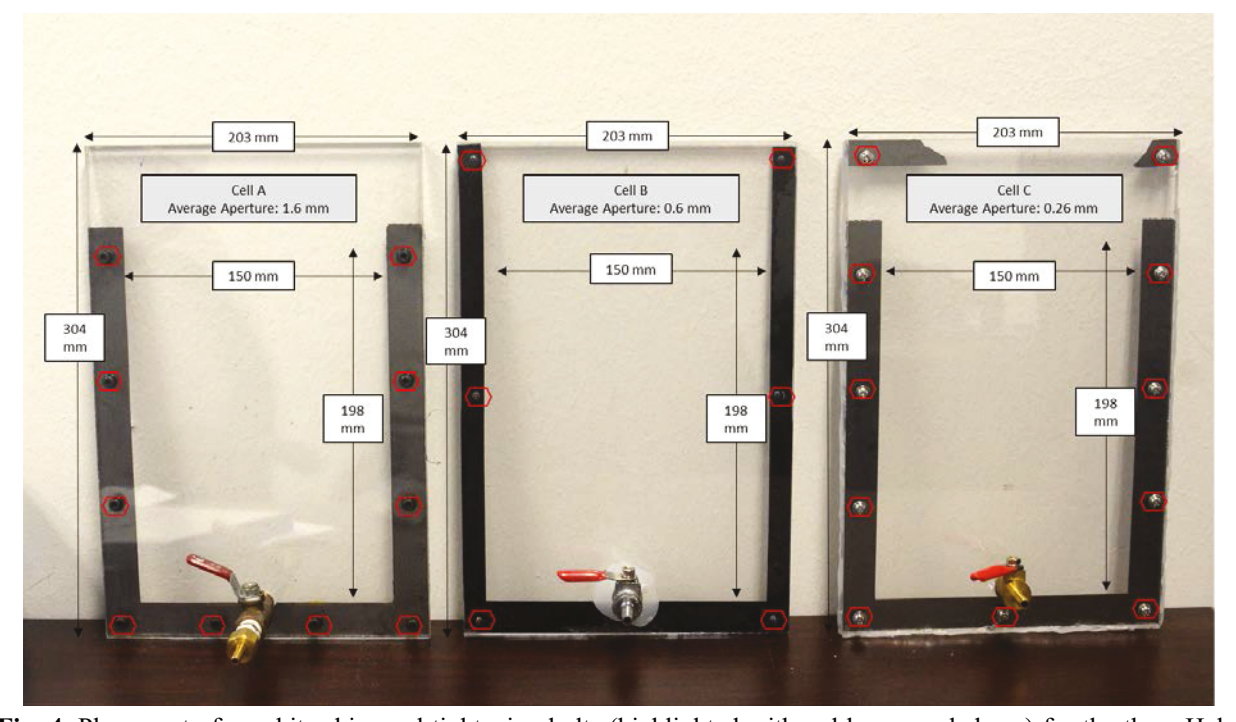


Fig. 4. Placement of graphite shim and tightening bolts (highlighted with red hexagonal shape) for the three Hele-Shaw cells considered in this study.

In contrast, alongside graphite shims up to the water level, shims were also placed at the top boundaries of cell C, shown in **Fig. 4**. By doing so, another variation of the permeability heterogeneity was obtained with slightly lower permeability at the top of the cell, as shown in **Fig. 3** (c).

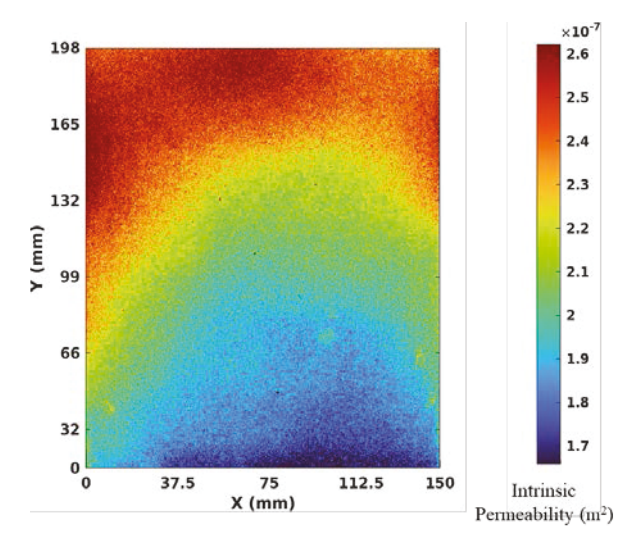


Fig. 5. Permeability map for cell A at a uniform bolt tightening force

Finally, silicone shims were placed along the sidewalls of cell B, which are more flexible than graphite shims, leaving additional space for tightening the bolts. Based on our previous study, graphite exhibited higher adhesion to the cell wall compared to silicone; therefore, by using silicone shims with tightening bolts placed far apart, a non-uniform aperture can be obtained close to the shim regions, as evident by the permeability map for cell B shown in **Fig. 3 (b)** [20]. Also, it is worth noting that the shim materials are merely a boundary, and using different shim materials does not affect any surface flow properties of the cell (e.g., interfacial tension, wettability, etc.) [20].

5. Qualitative Visualization

This section presents the qualitative visualization of CO₂ density-driven convective transport on cells A, B, and C. The complex permeability distribution of these cells allows for visualization of the effect of permeability contrast on the convective transport of CO₂.

5.1. Qualitative Visualization for Cell A (Ra number 86,816)

Upon injection of gaseous CO₂ at a continuous flow rate of 0.59 L/min using the top injection port of the cell, the CO₂

dissolves into the solution via diffusion, which is the only applicable mechanism at the initial stage. The diffusive layer at the gas-water interface gradually increases without deformation or instability. Fig. 6 shows the onset of the convection process by focusing on the changes near the gas-water interface for different timescales. For cell A (average aperture of 1.6 mm), at around 114 seconds, slight perturbations in the CO₂ diffusive layer can be observed, thus indicating the onset of density-driven instability, as shown in Fig. 6. However, it is worthwhile to note that although the perturbations are clearly observed at 114 seconds, it is merely the qualitative onset of convection. The actual onset of density-driven instability, commonly referred to as the quantitative onset of convection, occurs sooner, although not visible to the naked eye [14,20].

The perturbation increases in vertical depth, causing it to form finger-like shapes, which are clearly observable around 130 seconds. Compared to the experiment period indicated by the time the CO₂ reaches the bottom of the cell or 150 minutes, whichever is faster- the onset of the convective mechanism in dissolution in CO₂ happens at the early stage in a short time. Moreover, the change from the primary diffusion-driven dissolution mechanism to the onset of the convection process happens a few millimeters down from the gas-water interface, thus making the process rather hard to capture accurately.

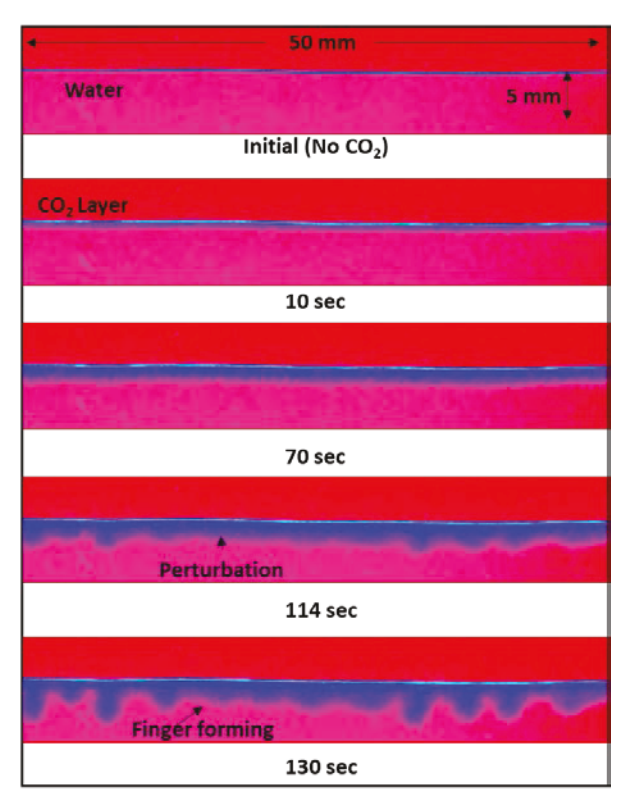


Fig. 6. Qualitative onset of convection for cell A

Fig. 7 shows the successive snapshots for cell A. As shown in **Fig 7**, the spectrum-based lookup based on a blue color channel with a scale of 0-255 is applied as the primary image processing method, allowing us to differentiate between the subtle variations of CO₂ concentration in different regions of the Hele-Shaw cell. CO₂ dissolution region ranges from around 130 to 180 on the color scale, where a lower value in the color scale indicates a higher concentration. As observed in **Fig. 7**, the CO₂-water interface region has a relatively high concentration of CO₂ throughout the experiment. Moreover, the middle of the finger-shaped plumes has a higher CO₂ concentration than the boundary. Furthermore, the highly concentrated regions merge and keep moving vertically downwards, clearly observable in **Fig. 7** (e) and (f). Similar patterns of concentration distribution were reported in the simulation of Zhang et al. [29]. Furthermore, their investigation in the gap direction showed a lower concentration boundary outside of the convective fingers, which could be attributed to an effect of gap-induced dispersion. However, it should be noted that their work considers an aperture of 3 mm and, therefore, will have considerably higher gap-induced flow behavior compared to our study [29].

As shown in **Fig. 7**, the formation of nascent fingers throughout the experiment is observable, evident by tiny oval-shaped regions with low color scale values at the gas-water interface.

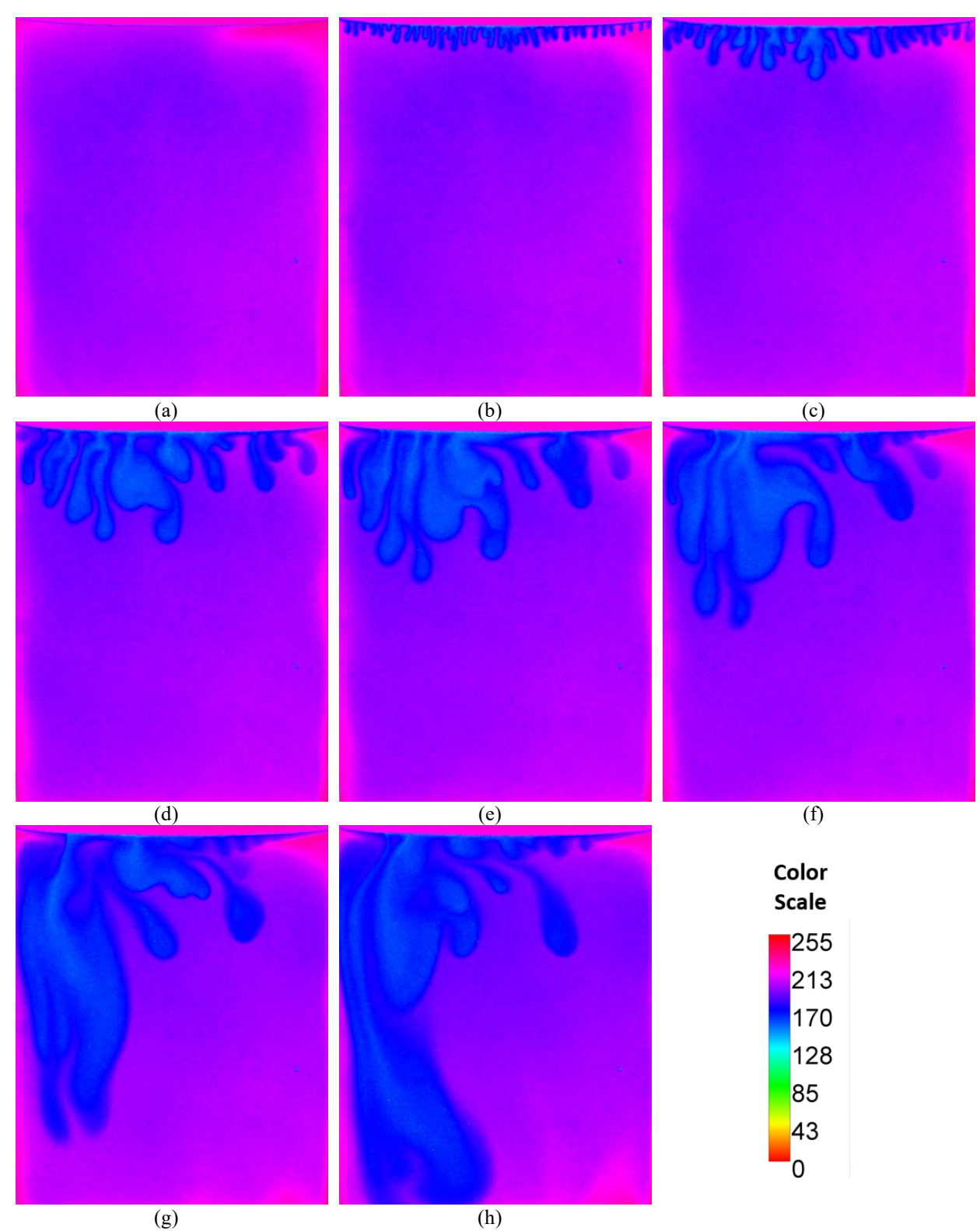


Fig. 7. CO₂ introduced to the middle of cell A(a) Initial (no CO₂) (b) 5 minutes (c) 10 minutes (d) 20 minutes (e) 25 minutes (f) 30 minutes (g) 40 minutes (h) 50 minutes.

The fingers grow in width and depth with time, eventually merging into longer and thicker fingers. However, rather than a uniform vertical traverse throughout the Hele-Shaw cell, the finger growth rate differs for different cell

regions. This becomes evident in the later part of the experiment, as shown in **Fig. 7.** This non-uniform finger flow regime can be attributed to the effect of heterogeneities present in the Hele-Shaw cell. As shown in **Fig. 3 (a)**, cell A has a higher permeable region in the upper-middle section of the left side of the cell, which can explain the tendency of finger movement in that region. It should be noted that although the range of permeability distribution (around 1×10^{-7} m²) is not considerably high, and the small change in permeability can cause huge effects in dictating the dissolution flow pattern.

5.2. Qualitative Visualization for Cell B (Ra number 12,279)

 Although cell B (average aperture of 0.6 mm) exhibits a similar onset of convection phenomenon after a certain diffusion-driven period, the time frame for disturbance in the diffusive layer and first observance of finger formation is much slower. Rather than observing initial finger formation throughout the entire diffusive layer at the same time, we observe early finger formation at the side of the Hele-Shaw cell (at 158 sec) compared to the middle (698 sec), as shown in **Fig. 8**. The raw images for **Fig. 8** were color adjusted and presented without performing spectrum lookup, as it exhibited the best visualization in this scenario. This early finger formation can be attributed to different permeable regions, as observed in the permeability map shown in **Fig. 3** (b). Regions with low permeability (middle of the Hele-Shaw cell) have a delayed onset of convection, whereas, at higher permeability regions (side of the cells), the onset of convection happens earlier.

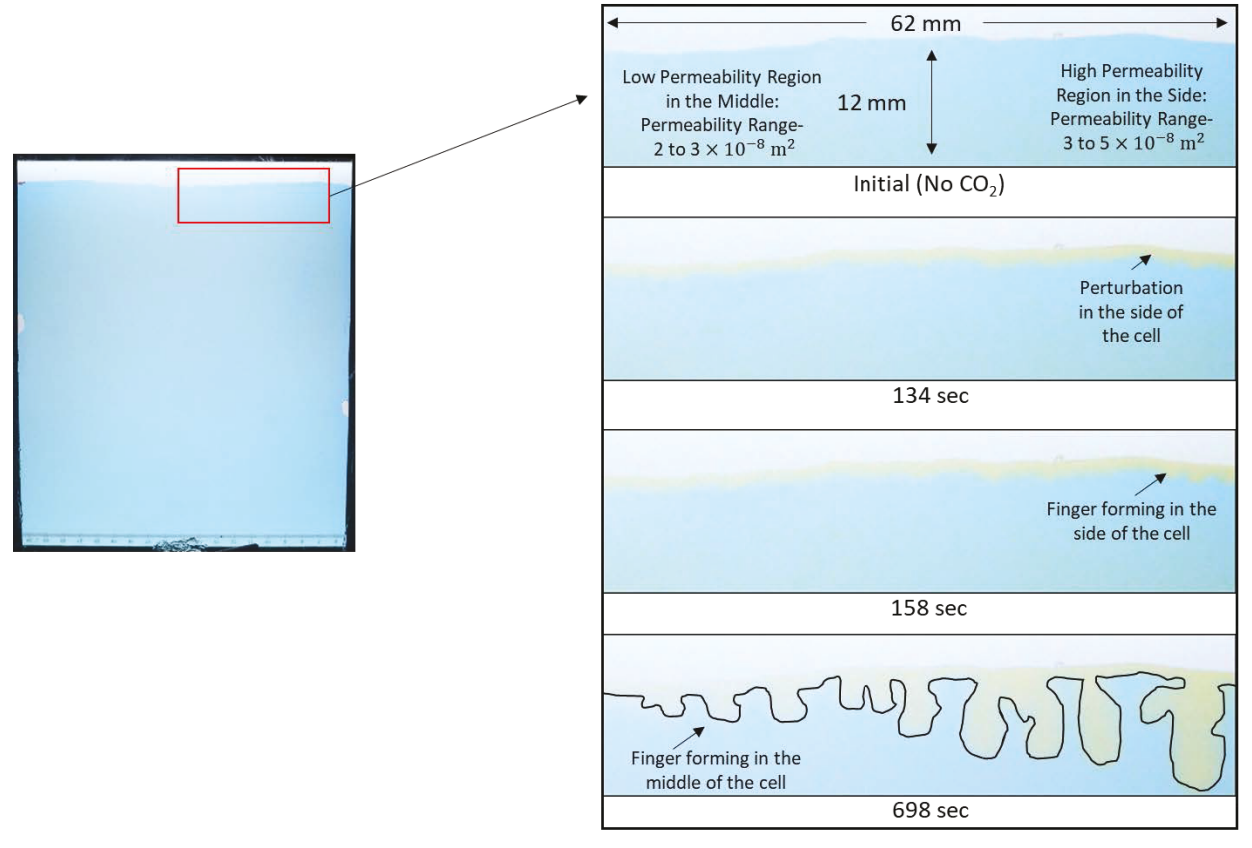


Fig. 8. Qualitative onset of convection for cell B. The raw images were color adjusted and presented without spectrum lookup, and the boundary of fingers in the bottom picture is manually drawn for better visualization.

The varied growth rate becomes more apparent as time progresses, as evident in **Fig. 9.** The middle side of the Hele-Shaw cell has a lower permeability region, resulting in a slower growth rate. In contrast, higher permeable regions on the side contribute to faster growth. The permeability variation thus leads to preferential finger movement rather than uniform vertical travel. Similar phenomena were observed in the heterogeneity-based experiments in our previous work [20].

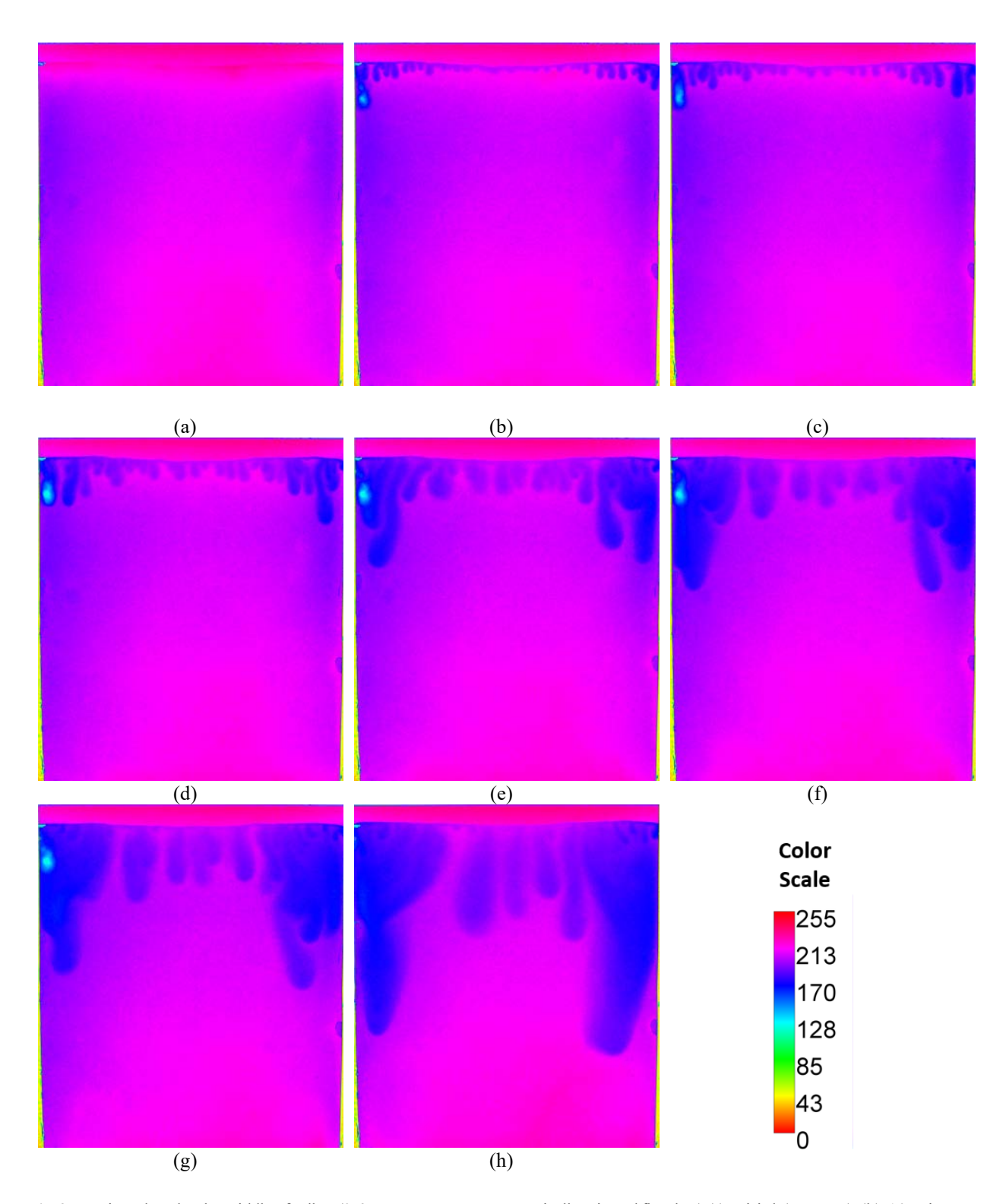


Fig. 9. CO₂ introduced to the middle of cell B (0.6 mm average aperture, vertically oriented flat glass)(a) Initial (no CO₂) (b) 10 minutes (c) 15 minutes (d) 25 minutes (e) 50 minutes (f) 70 minutes (g) 90 minutes (h) 150 minutes.

A visual comparison between cell A (Ra 86,816) and cell B (Ra 12,279) reveals that the fingers reach the bottom of the cell at around 50 minutes in cell A. In contrast, even around 150 minutes, the fingers do not reach the bottom of

cell B. This shows that the finger growth rate increases at a higher Rayleigh number, which is in agreement with Riaz et al. [67] and Faisal et al. [31], who observed more vigorous finger interaction in higher Rayleigh numbers.

5.3. Qualitative Visualization for Cell C (Ra number 2389)

The slowest finger growth rate is observed in cell C. The beginning of the finger shape is noticeable around 18 minutes,

as shown in **Fig. 10.** This delayed qualitative onset time of convection can be attributed to the low permeability and corresponding low Ra number (Ra = 2389). Any clear form of perturbation was difficult to visualize in this scenario since the instability in the diffusive layer was not as sharp as in the previous heterogeneous models. The qualitative onset of convection observed for the cells in this study, reported in **Table 4**, shows that qualitative onset of convection is observed earlier on high Ra number scenarios, which agrees with previous studies [14,31,68].

Considerably slower vertical movement is observed in this model, which, coupled with lateral mixing between fingers, gives rise to plume-shaped uniform movement, as observed in Fig. 11. The number of fingers formed is also lower in this heterogeneous model; however, they are relatively thicker, even at earlier times of the experiment.

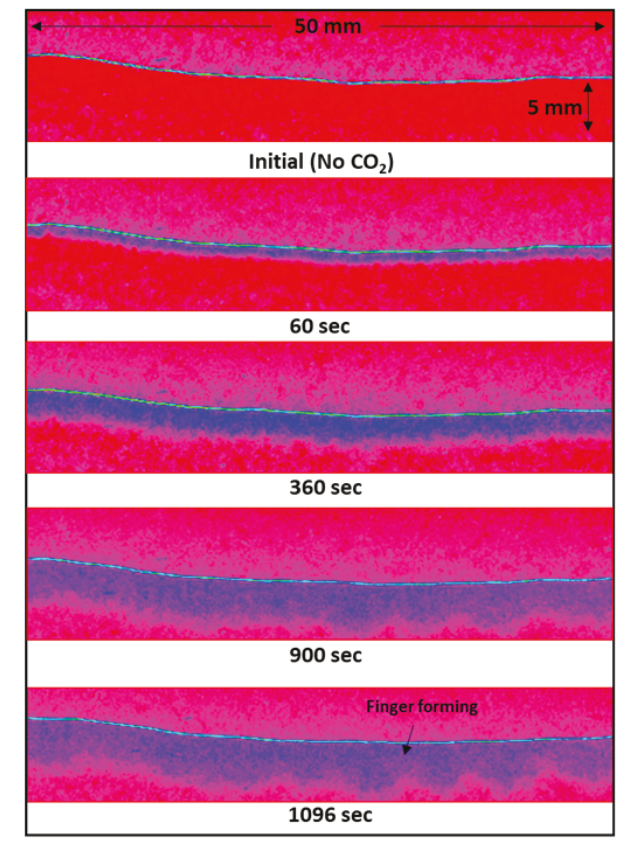


Fig. 10. Qualitative onset of convection for cell C

Table 4. Qualitative onset of convection observed for the cells in this study

		•		•
Hele-Shaw cell Considered	Average Aperture	Ra number	Initial Perturbations observed around	Formation of fingers observed around (qualitative onset of convection)
Cell A	1.6 mm	86,816	114 sec	130 sec
Cell B	0.6 mm	12,279	134 sec ^a	158 sec ^a
Cell C	0.26 mm	2389	Not clearly visible ^b	1096 sec ^b

 ^aObserved at the high permeability region of the cell; ^b Clear formation of perturbation or fingers was challenging to visualize in this scenario since the instability in the diffusive layer was not as sharp as in the previous cases

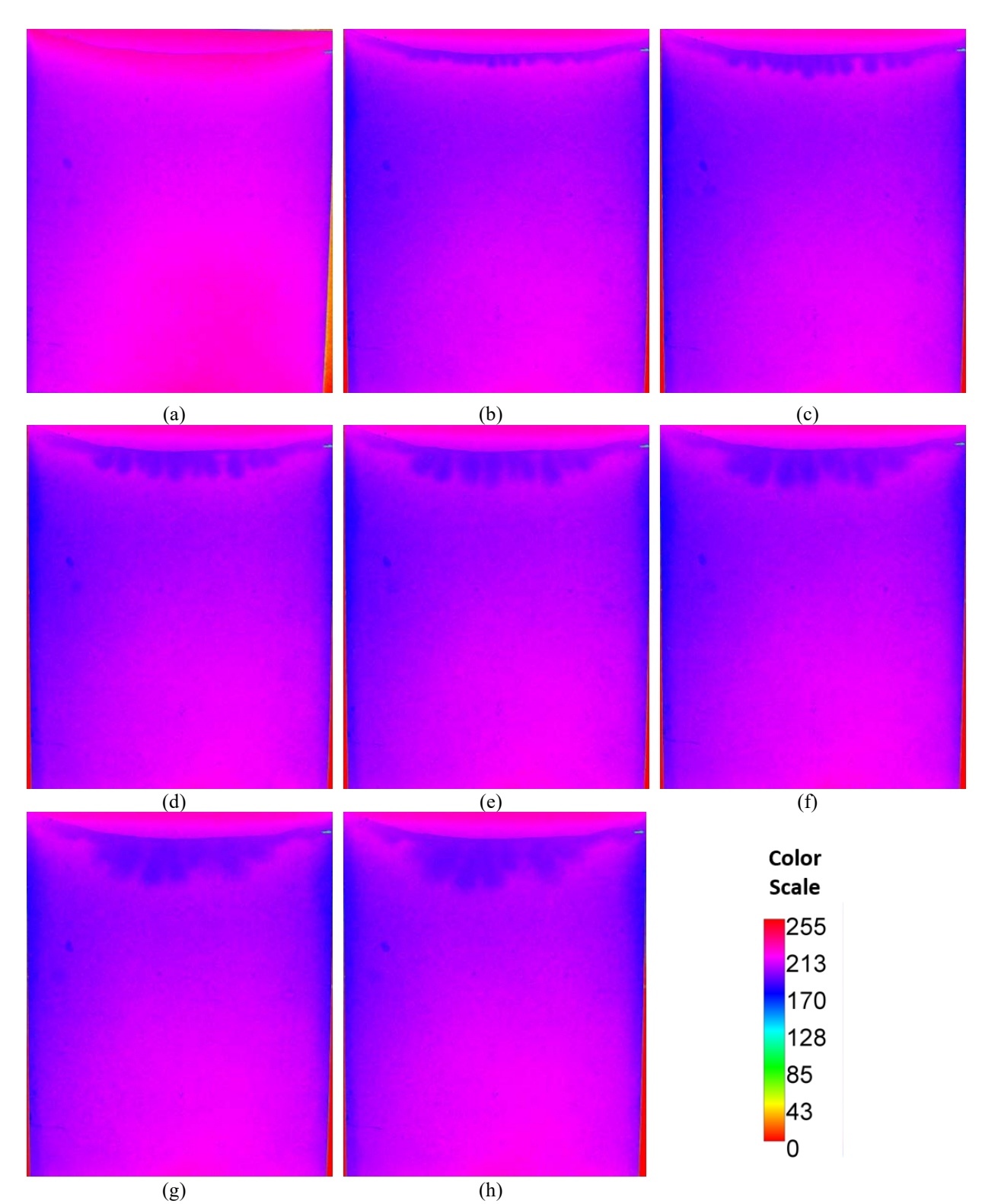


Fig. 11. CO₂ introduced to the middle of cell C (0.6 mm average aperture, vertically oriented flat glass) (a) Initial (no CO₂) (b) 25 minutes (c) 45 minutes (d) 65 minutes (e) 85 minutes (f) 105 minutes (g) 125 minutes (h) 150 minutes.

Based on the qualitative visualization, more vigorous finger interaction, faster vertical travel, and overall dissolution are observable in higher Rayleigh number scenarios. The fingers are more uniformly shaped in plume form in lower

Ra numbers. The permeability change throughout the region of interest was found as a major parameter in dictating finger morphology through preferential finger movement. Furthermore, the preferential dissolution path showed poor sweep efficiency in low-permeable regions. This further emphasizes the importance of accounting heterogeneities, albeit small, in experiments and numerical simulations.

6. Quantitative Characterization

6.1. Vertical Progression of Fingers

Faster vertical travel of CO₂ dissolved region is preferable in CO₂ sequestration operations as it promotes quick CO₂ sinking rather than rising to shallower formations. The temporal evolution of fingers in cells A, B, and C is presented in Fig. 12 (a). Using ImageJ, the vertical distance traveled is calculated from the gas-water interface to the tip of the longest finger in each case. The observed finger growth is nonlinear for all the cells. After a short diffusion stage, a sharp increase in finger length in cells A and B indicates the effect of convective dissolution. Moreover, in cell B, the finger growth is considerably higher in the more permeable regions (at the side of the cell) compared to the less permeable region (middle of the cell). However, cell C exhibits gradual finger growth, showing that the effect of convective flow is lower in low permeability conditions.

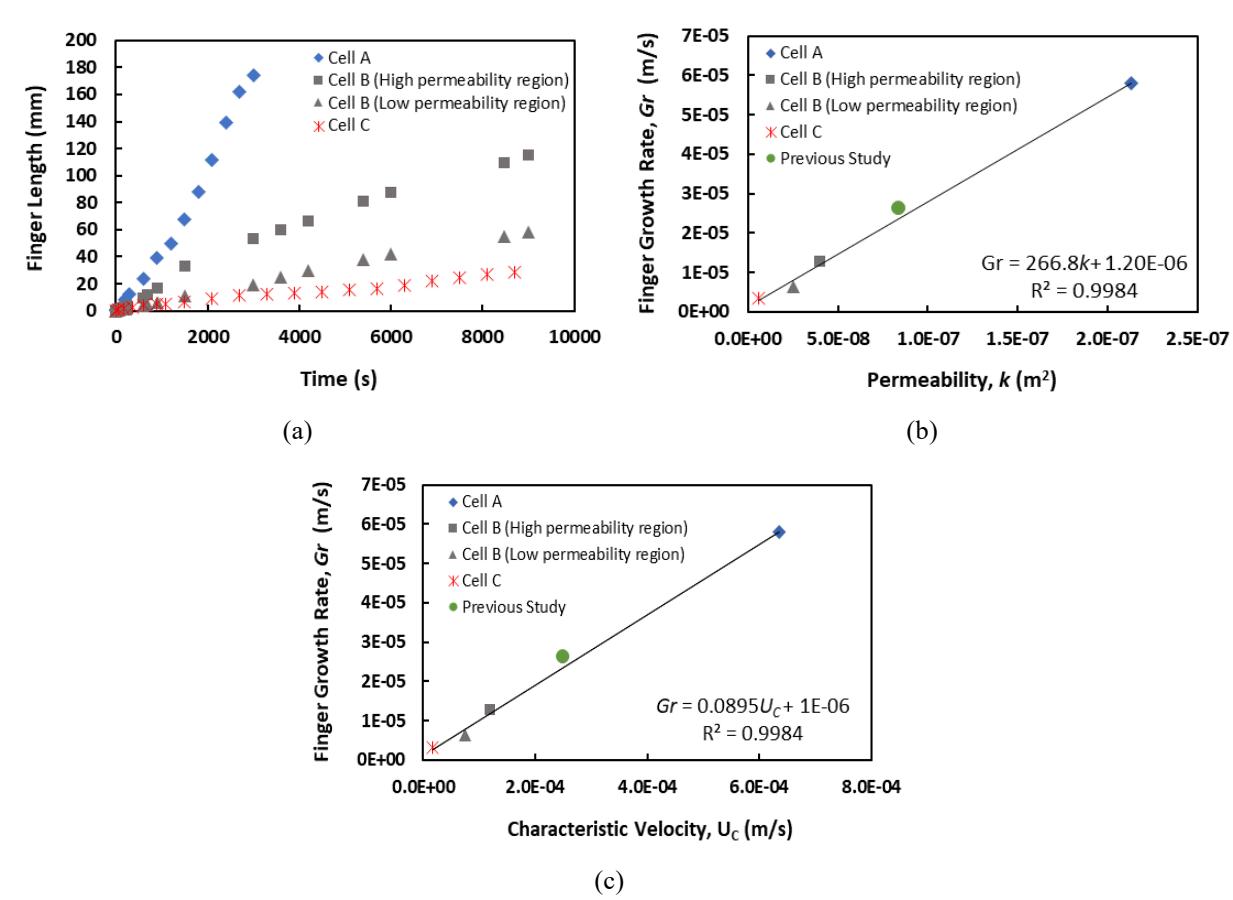


Fig. 12. (a) Temporal evolution of finger length in cells A, B, and C; Scaling relationship between (a) finger growth rate and cell permeability (c) finger growth rate and characteristic velocity (Previous study refers to the work of Shahriar and Khanal [20])

The effect of permeability in dictating finger growth is more evident in **Fig. 12 (b)**, which illustrates the relationship between finger growth rates with respect to permeability. The finger growth rate is calculated as the ratio of the maximum vertical distance traveled by the longest finger (calculated using ImageJ) and the time taken to reach the bottom of the cell or the experimental time duration (2.5 hours), whichever is shorter. A scaling relationship between the value of finger growth rate (Gr) and permeability (k) is established using a linear fit. Here, Gr scales with k as follows:

$$Gr(m.s^{-1}) = 266.8k(m^2) + 1.20 \times 10^{-6}$$
 (12)

Fig. 12 (c) shows that the finger growth rate is also proportional to the characteristic Darcy velocity U_C , expressed as follows:

$$Gr(m.s^{-1}) = 0.0895U_C(m.s^{-1}) + 1 \times 10^{-6}$$
 (13)

A similar proportional relationship between finger growth velocity (calculated using the migration distance of the rising fingertip) and characteristic Darcy velocity was also observed in the work of Teng et al. [69]. The evolution equation of characteristic Darcy velocity can be represented in Eq. 14 [23,26].

$$U_C = \frac{\Delta \rho g k}{\mu} \tag{14}$$

As shown in Fig. 12 (b and c), the proposed relationships (Eq. 12 and 13) show a good prediction of independent experimental data generated in our prior study [20]. The prior study used a homogenous Hele-Shaw cell with an average aperture and water column height of 1 mm and 242.88 mm, respectively, where the longest finger reaches the bottom of the cell in 154 minutes [20]. As observed in Fig. 12 (b), the growth rate can be well explained by the scaling relationship obtained. Furthermore, based on this and previous studies, it can be seen that despite heterogeneity, CO₂ fingers will have a preferential path based on permeability with a corresponding growth rate, making it comparable with a homogenous medium [20,70]. This statement is also supported by the work of Green and Ennis-King [70], where scaling analysis pertaining to a simple heterogeneity model was also applicable for anisotropic homogeneous porous media. Further studies on the vertical growth rate are needed to make justified assumptions on the strength of a particular geological CO₂ storage site.

6.2. Mass of Dissolved CO₂

The spectrophotometric method was employed to quantify the mass of CO₂ dissolved [39,40]. Although previous studies considered grayscale models for quantitative characterization, this study analyzes the three different color channels, which are more effective for characterizing the flow in Hele-Shaw cells [38]. This technique uses the Beer-Lambert law (Eq. 8), which relates the variation of light attenuation based on the property of the material it travels through. Thus, by using a monochromatic light source and noticing the changes in light intensity values after it passes through the Hele-Shaw cell, CO₂ dissolution was characterized. ImageJ was used to convert each image into separate color channels before analysis. The light source in this study was powered by DC current, and the light intensity values were averaged based on three pictures, taken for the spectrophotometric analysis.

When CO_2 reacts with H_2O , it forms carbonic acid (H_2CO_3), further dissociating into carbonate CO_3^{2-} and bicarbonate HCO_3^{-} ions instantaneously, as expressed by the following equations:

$$CO_2(g) = CO_2(aq) \tag{15}$$

$$CO_2(aq) + H_2O = H^+ + HCO_3^-$$
 (16)

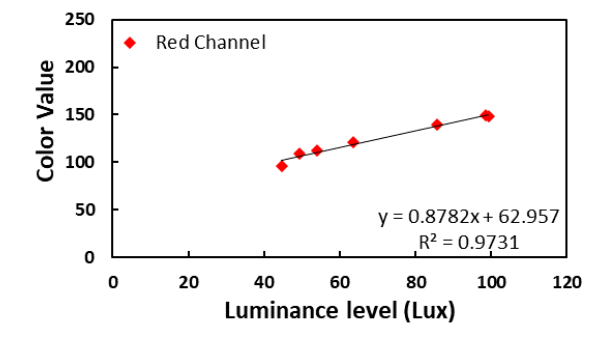
$$HCO_3^- \leftrightharpoons H^+ + CO_3^{2-}$$
 (17)

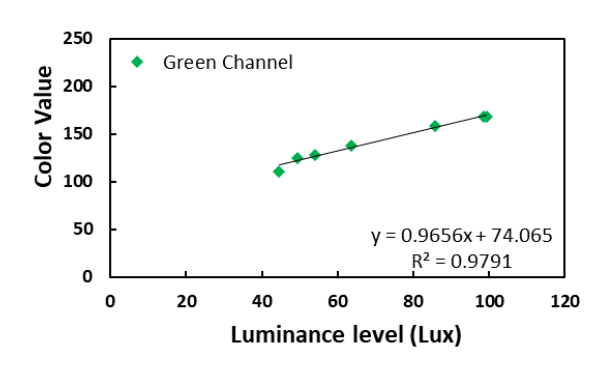
Eq. 17 is neglected for convenience of calculation, as the equilibrium constant of Eq. 17 is several orders of magnitude smaller than that of Eq. 16 [40]. By calculating the luminous intensity of the cell with and without solution, the absorbance. A can be calculated as follows:

$$A = \log_{10} \frac{I_{\nu_0}}{I_{\nu_0}} \tag{16}$$

Where I_{y0} and I_y are the luminous intensity passing through the Hele-Shaw cell without and with the solution.

By controlling the output light brightness, different luminance level (L_l) conditions were obtained, under which the color value of three different channels (Red, Green, and Blue) in the region of interest (ROI) were measured, as shown in **Fig. 13**.





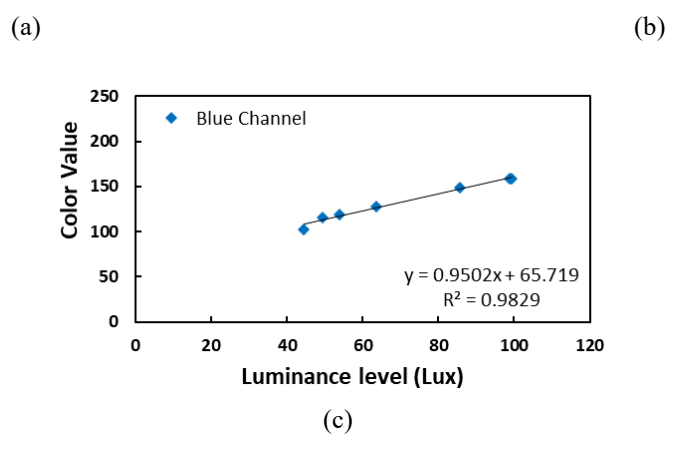


Fig. 13. The relationship between color value and luminance level at the region of interest for (a) red channel, (b) green channel, and (c) blue channel

498 499 500

501

502

503 504

505

507

508

509

511

513

514

515

516 517

518

519

520

524

525

Fig. 13 shows that the blue channel holds the best linear relationship with luminance level, expressed in Eq. 19 and thus considered in subsequent spectrophotometric calculations. Furthermore, the maximum luminance level obtainable from the light source $L_l = 100$ lux is selected as the incident light source luminance.

$$B = 0.95L_1 + 65.719, L_1 \in [40, 100] \tag{19}$$

By combining Eq. 18 and 19 and replacing the ratio of luminous intensity with the ratio of luminance level, the absorbance A can be expressed as follows:

$$A = -\lg\left(\frac{B - 65.719}{B_0 - 65.719}\right) \tag{20}$$

where, B_0 and B is the blue color channel value in the region of interest of the Hele-Shaw without and with solution, respectively. The pH indicator molecules exhibiting acid-base properties can be divided into the acidic form (HIn) and conjugate base form (In⁻). The equilibrium equation for the indicator is as follows:

$$HIn = H^{+} + In^{-}$$
 (21)

Where the equilibrium constant of Eq. 21 can be expressed as:

$$\lg(K_{\text{HIn}}) = \lg\left(\frac{[\text{In}^-]}{[\text{HIn}]}\right) - \text{pH}$$
 (22)

Where the molar concentration of species is specified inside the square brackets []. When CO₂ starts dissolving in the solution, the hydrogen ions (H⁺) released from CO₂ dissolution change the ratio of [HIn] and [In⁻] in the solution, causing the color change in the solution. The absorbance of the indicator in a strong acid or strong alkali environment can be expressed by the following equations:

$$A[HIn] = \alpha_0. b. [HIn] = \alpha_0. b. c$$
 (23)

$$A[In^{-}] = \alpha^{-}.b.[In^{-}] = \alpha^{-}.b.c$$

$$(24)$$

Where c is the concentration of the pH indicator. Using the extreme absorbance values and Eq. 20, 21, and 22, the following equation is derived:

$$\lg\left(\frac{A - A_{[HIn]}}{A_{[In^-]} - A}\right) = pH - pK_{HIn}$$
 (25)

Where $\lg \left(\frac{A - A_{[HIn]}}{A_{[In-]} - A} \right)$ is absorbance factor which varies proportionally with the solution pH. By adding different 522 523

concentrations of hydrochloride acid or sodium hydroxide, the pH of the experimental solution was varied within the functional range of the pH indicator, and the corresponding absorbance factor was calculated, as presented in Fig. 14.

Using pH = 10 and pH = 1 solution, extreme absorbance values $A[In^-]$ and A[HIn], were calculated.

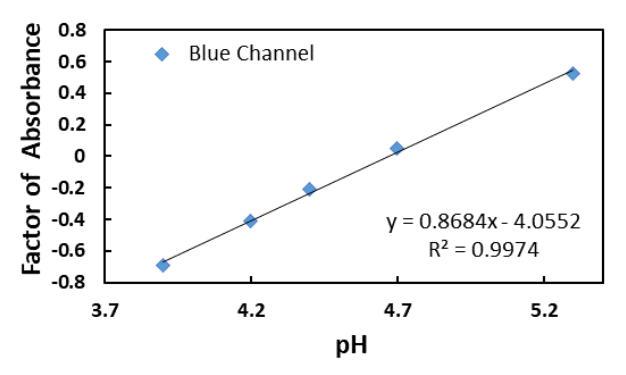


Fig. 14. The linear relationship between the factor of absorbance and pH using blue channel absorbance values.

As shown in **Fig. 14**, the factor of absorbance $\left(\lg\left(\frac{A-A_{[HII]}}{A_{[In-]}-A}\right)\right)$ has a good linear fit with the pH of the solution. The following charge balance equation can be used to explain the electrical neutrality in the solution.

$$[HCO_3^-] + [In^-] = [H^+]$$
 (26)

Using Eq. 22 and 23 and taking pH indicator concentration as $c = 1.63 \times 10^{-4}$ mol/L, [In⁻] can be expressed as:

$$[In^{-}] = \frac{c}{10^{-pH} \cdot K_{HIn}^{-1} + 1}$$
 (27)

Using the standard curve from Fig. 14 and using Eq. 25 and 26, $[HCO_3^-]$ can be calculated. Moreover, combining the equilibrium expression involving CO_2 and reaction equilibrium constant, the following equation is derived:

$$[CO_2(aq)] = \frac{[HCO_3^-].[H^+]}{K_{CO_2(aq)}}$$
(28)

(b)

The total dissolved CO₂ concentration is expressed as follows:

(a)

$$[CO2(dissolved)] = [CO2(aq)] + [HCO3-]$$
(29)

In order to ensure the accuracy of the method, solutions of known pH values were obtained using different concentrations of NaOH or HCl and compared with calculated pH values from the factor of absorbance vs. pH curve (from Fig. 14). The calculated cumulative dissolved CO_2 mass was also compared to the dissolved CO_2 mass just by diffusion. The mass transport due to diffusion M(t) was obtained using Fick's law, as shown in Eq. 30 [37].

Fig. 15. (a) Cumulative dissolved CO_2 mass as a function of time (b) Change in flux throughout the experimental time where C_0 is the solubility of CO_2 in solution. Fig. 15 (a) shows the cumulative mass of CO_2 stored compared with the mass of CO_2 stored by just diffusion, whereas the cumulative and diffusive flux is presented in Fig. 15 (b). The

dissolution in the early stages of the experiment was purely diffusion-based, thereby making it difficult to record the small amount of CO₂ dissolved at the early stages of the experiment. Thus, the diffusion-dominated region mass flux was calibrated using Eq. 30 in the spectrophotometric method. A higher amount of CO₂ is observed to be dissolved throughout the experiment compared to the amount obtained by the diffusion equation (Eq. 30), where the discrepancy can be attributed to the effect of CO₂ dissolution due to convective flow [14.31.71]. The maximum Sherwood number, Sh, expressed as the ratio of the convective mass flux (difference between the maximum experimental dissolution flux and diffusive flux, shown in Fig. 15b) and diffusive mass flux, was calculated as 6.8. Although the Sh observed in this study is lower than existing studies [30,72], it is worthwhile to point out that we observed an increase in the dissolution flux at the later stage of the experiment (Fig. 15). This result indicates a potentially higher Sh number, similar to existing studies, if the experiment was continued for a longer time period. However, this was not possible with the current experimental setup as the CO₂ fingers reached the bottom of the cell after which the experimental was terminated. As observed in Fig. 15, while the diffusive flux decreases throughout time, the convective flux seems to vary, which can be attributed to the spatial heterogeneity of the medium, as observed in the work of Green and Ennis-King [73]. Similar dissolution flux behavior was reported in the work of Slim et al. [36], where a sudden rise in flux was reported and termed as 'flux growth" regime, which is observed after around 500 sec in our work (Fig. 15 (b)). The drop in dissolution flux after the flux growth regime was considered to be the onset of "merging" regime, observed in about 30 minutes in our study as seen in Fig. 15 (b). Although their study experienced a steady-flux regime in the later stage, we do not observe that as the fingers reach the bottom of the cell before reaching the constant dissolution flux phase.

7. Summary and Conclusion

This study explored CO₂ dissolution in complex heterogeneous media in three heterogeneous cells with varying average permeability. By creating complex heterogeneity, i.e., irregular permeability variations throughout the cell, the obtained CO₂ finger morphology mimics the actual storage geological storage sites. The finger movement path was non-uniform due to spatial heterogeneity, resulting in preferential finger movement toward high permeability regions. In contrast, lower permeable regions had minimum dissolution, leading to poor sweep efficiency. More vigorous vertical finger movement was observed for cells A and B, while cell C showed slowed vertical movement. Furthermore, higher permeability led to a faster onset of convection, which is also preferable for safe CO₂ storage. Although this study considers the CO₂ convective-dissolution flow behavior in complex heterogeneity conditions, future studies will consider a more complicated experimental approach to gain higher control over permeability variation inside the Hele-Shaw cell.

The image processing method helped identify the high CO₂ concentrated regions, particularly in the center of the fingers and at the gas-water interface. The shape of the CO₂ dissolution region also varied based on average cell permeability; while cells A and B had a more prominent finger-like shape alluding to the effect of faster vertical travel, cell C was shaped like a plume, which can be attributed to slower vertical travel promoting lateral mixing. The qualitative visualization revealed the gas-water interface and the middle of the finger-shaped dissolved regions having higher CO₂ concentration than the dissolved area's boundary. The results of the experiments are also characterized using several dimensionless numbers and will hold for other systems with the same dimensionless numbers.

Although previous studies using the spectrophotometric method obtained correlations using the gray channel, this study analyzed based on three color channels and concluded that the blue color channel holds the best linear relationship with respect to pH change. Based on our literature survey, there have been only two studies on the spectrophotometric technique, necessitating further studies to improve this method. Based on the results from the spectrophotometric analysis, the convective flux of cell A showed variation because of the spatial heterogeneity of the medium. A scaling relationship between the average finger growth rate (Gr) and permeability (k) was established as $Gr\left[m.s^{-1}\right] = 266.8k\left[m^2\right] + 1.20 \times 10^{-6}$. Using spectrophotometric analysis, dissolved CO₂ mass was calculated throughout time and was compared with mass transfer just by diffusion, with a maximum Sherwood number of 6.8 for cell A. Additionally, the dissolution flux was identified, and the effects of heterogeneity on unsteady mass flux were observed. Further laboratory studies are needed to investigate the role of permeability heterogeneity in CO₂ dissolution. The findings of this study will add to the existing knowledge of heterogeneity effects on density-driven convective transport.

Acknowledgements:

We want to thank Mr. Edward Farina from the UT Tyler Machine Shop for his significant help with the material selection, fabrication, and troubleshooting of the apparatus used in this study. We thank the anonymous reviewers for their edits and suggestions, which improved our manuscript. This material is based upon work supported in part by the National Science Foundation Award under CBET-2245484 and in part by the U.S. Department of Energy, Office

of Science, Basic Energy Sciences' Geoscience program under Award Number DESC0024642. Any opinions
findings, conclusions, or recommendations expressed in this material are those of the author(s) and do not necessarily
reflect the views of the funding agencies.

References

605

- Earth System Research Laboratories, Global Monitoring Laboratory, 2023. (n.d.). https://gml.noaa.gov/ccgg/trends/monthly.html (accessed June 8, 2023).
- 608 [2] F. Aldred, N. Gobron, J.B. Miller, K.M. Willett, R. Dunn, Global climate, Bull. Am. Meteorol. Soc. 102 (2021) S11–S142. https://doi.org/10.1175/BAMS-D-21-0098.1.
- A.B. Smith, NOAA National Centers for Environmental Information, U.S. Billion-Dollar Weather Clim.
 Disasters, 1980 Present (NCEI Access. 0209268). (2020). https://doi.org/https://doi.org/10.25921/stkw-7w73.
- M.F. Shahriar, A. Khanal, The current techno-economic, environmental, policy status and perspectives of sustainable aviation fuel (SAF), Fuel. 325 (2022) 124905. https://doi.org/10.1016/j.fuel.2022.124905.
- 615 [5] A. Khanal, M.F. Shahriar, Physics-Based Proxy Modeling of CO2 Sequestration in Deep Saline Aquifers, Energies. 15 (2022) 4350. https://doi.org/10.3390/en15124350.
- A. Khanal, M.F. Shahriar, Optimization of CO2 Huff-n-Puff in Unconventional Reservoirs with a Focus on Pore Confinement Effects, Fluid Types, and Completion Parameters, Energies. 16 (2023) 2311. https://doi.org/10.3390/en16052311.
- D. Li, Y. Zhong, X. Jiang, Experimental study of impurity effects on convective mixing in Hele-Shaw cell with application to CO2 geological sequestration, Adv. Water Resour. 172 (2023). https://doi.org/10.1016/j.advwatres.2023.104379.
- 623 [8] C. Fu, Y. Du, W. Song, S. Sang, Z. Pan, N. Wang, Application of automated mineralogy in petroleum geology 624 and development and CO2 sequestration: A review, Mar. Pet. Geol. 151 (2023). 625 https://doi.org/10.1016/j.marpetgeo.2023.106206.
- Y. Tang, Z. Li, R. Wang, M. Cui, X. Wang, Z. Lun, Y. Lu, Experimental Study on the Density-Driven Carbon
 Dioxide Convective Diffusion in Formation Water at Reservoir Conditions, ACS Omega. 4 (2019) 11082–11092. https://doi.org/10.1021/acsomega.9b00627.
- 629 [10] R. Khosrokhavar, G. Elsinga, R. Farajzadeh, H. Bruining, Visualization and investigation of natural 630 convection flow of CO2 in aqueous and oleic systems, J. Pet. Sci. Eng. 122 (2014) 230–239. 631 https://doi.org/10.1016/j.petrol.2014.07.016.
- R. Khosrokhavar, A. Eftekhari, R. Farajzdadeh, K.H. Wolf, H. Bruining, Effect of Salinity and Pressure on the Rate of Mass Transfer in Aquifer Storage of CO2, IOR 2015 - 18th Eur. Symp. Improv. Oil Recover. (2015). https://doi.org/10.3997/2214-4609.201412114.
- H. Emami-Meybodi, Stability analysis of dissolution-driven convection in porous media, Phys. Fluids. 29 (2017). https://doi.org/10.1063/1.4974275.
- 637 [13] C.A. Dorao, Dispersion phenomena in gas liquid systems, J. Nat. Gas Sci. Eng. 5 (2012) 25–30. 638 https://doi.org/10.1016/j.jngse.2011.08.004.
- A. Taheri, O. Torsæter, E. Lindeberg, N.J. Hadia, D. Wessel-Berg, Qualitative and quantitative experimental study of convective mixing process during storage of CO2 in heterogeneous saline aquifers, Int. J. Greenh. Gas Control. 71 (2018) 212–226. https://doi.org/10.1016/j.ijggc.2018.02.003.
- A. Taheri, O. Torsæter, D. Wessel-Berg, M. Soroush, Experimental and Simulation Studies of Density-Driven-Convection Mixing in a Hele-Shaw Geometry with Application for CO2 Sequestration in Brine Aquifers, in: All Days, SPE, 2012. https://doi.org/10.2118/154908-MS.
- W. Amarasinghe, I. Fjelde, Y. Guo, CO2 dissolution and convection in oil at realistic reservoir conditions: A visualization study, J. Nat. Gas Sci. Eng. 95 (2021). https://doi.org/10.1016/j.jngse.2021.104113.
- W.S. Amarasinghe, I. Fjelde, A.M.N. Flaata, Visual investigation of CO2 dissolution and convection in heterogeneous porous media at reservoir temperature and pressure conditions, Greenh. Gases Sci. Technol. 11 (2021) 342–359. https://doi.org/10.1002/ghg.2055.
- L. Jiang, Y. Wang, G. Lu, J. Yang, Y. Song, Experimental Study on the Density-Driven Convective Mixing of CO2and Brine at Reservoir Temperature and Pressure Conditions, Energy and Fuels. (2022). https://doi.org/10.1021/acs.energyfuels.2c00054.
- B. An, D. Solorzano, Q. Yuan, Viscous Fingering Dynamics and Flow Regimes of Miscible Displacements in a Sealed Hele-Shaw Cell, Energies. 15 (2022) 5798. https://doi.org/10.3390/en15165798.
- 655 [20] M.F. Shahriar, A. Khanal, Fundamental investigation of reactive-convective transport: Implications for long-656 term carbon dioxide (CO2) sequestration, Int. J. Greenh. Gas Control. 127 (2023) 103916.

- https://doi.org/10.1016/j.ijggc.2023.103916.
- R. Outeda, C. El Hasi, A. D'Onofrio, A. Zalts, Experimental study of linear and nonlinear regimes of densitydriven instabilities induced by CO(2) dissolution in water, Chaos. 24 (2014) 013135. https://doi.org/10.1063/1.4868040.
- 661 [22] A. Singh, Y. Singh, K.M. Pandey, Viscous fingering instabilities in radial Hele-Shaw cell: A review, Mater. Today Proc. 26 (2019) 760–762. https://doi.org/10.1016/j.matpr.2020.01.022.
- 663 [23] M. De Paoli, M. Alipour, A. Soldati, How non-Darcy effects influence scaling laws in Hele-Shaw convection experiments, J. Fluid Mech. (2020). https://doi.org/10.1017/jfm.2020.229.
- M.C. Kim, Linear and nonlinear analyses on the onset of gravitational instabilities in a fluid saturated within a vertical Hele-Shaw cell, Chem. Eng. Sci. 126 (2015) 349–360. https://doi.org/10.1016/j.ces.2014.12.032.
- N. De, N. Singh, R. Fulcrand, Y. Méheust, P. Meunier, F. Nadal, Two-dimensional micromodels for studying the convective dissolution of carbon dioxide in 2D water-saturated porous media, Lab Chip. 22 (2022) 4645–4655. https://doi.org/10.1039/D2LC00540A.
- 570 [26] J.A. Letelier, H.N. Ulloa, J. Leyrer, J.H. Ortega, Scaling CO2 –brine mixing in permeable media via analogue models, J. Fluid Mech. 962 (2023) A8. https://doi.org/10.1017/jfm.2023.246.
- 672 [27] C. Wylock, A. Rednikov, B. Haut, P. Colinet, Nonmonotonic Rayleigh-Taylor Instabilities Driven by Gas– 673 Liquid CO 2 Chemisorption, J. Phys. Chem. B. 118 (2014) 11323–11329. https://doi.org/10.1021/jp5070038.
- K. Cao, M. Zhang, A.S. Mujumdar, Q. Zhong, Z. Wang, Effects of ultrasonic pretreatments on quality, energy consumption and sterilization of barley grass in freeze drying, 2018.
 https://doi.org/10.1016/j.ultsonch.2017.06.014.
- [29] Z. Zhang, Q. Fu, H. Zhang, X. Yuan, K.T. Yu, Experimental and Numerical Investigation on Interfacial Mass
 Transfer Mechanism for Rayleigh Convection in Hele-Shaw Cell, Ind. Eng. Chem. Res. 59 (2020) 10195–10209. https://doi.org/10.1021/acs.iecr.0c01345.
- 680 [30] S. Mojtaba, R. Behzad, N.M. Rasoul, R. Mohammad, Experimental study of density-driven convection effects 681 on CO2 dissolution rate in formation water for geological storage, J. Nat. Gas Sci. Eng. 21 (2014) 600–607. 682 https://doi.org/10.1016/j.jngse.2014.09.020.
- T.F. Faisal, S. Chevalier, Y. Bernabe, R. Juanes, M. Sassi, Quantitative and qualitative study of density driven CO2 mass transfer in a vertical Hele-Shaw cell, Int. J. Heat Mass Transf. 81 (2015) 901–914. https://doi.org/10.1016/j.ijheatmasstransfer.2014.11.017.
- H. Wang, F. Torabi, F. Zeng, H. Xiao, Experimental and numerical study of non-equilibrium dissolution and exsolution behavior of CO2 in a heavy oil system utilizing Hele-Shaw-like visual cell, Fuel. 270 (2020). https://doi.org/10.1016/j.fuel.2020.117501.
- 689 [33] M.C. Kim, C. Wylock, Linear and nonlinear analyses of the effect of chemical reaction on the onset of buoyancy-driven instability in a CO 2 absorption process in a porous medium or Hele-Shaw cell, Can. J. Chem. Eng. 95 (2017) 589–604. https://doi.org/10.1002/cjce.22694.
- 692 [34] S. Mahmoodpour, B. Rostami, M.R. Soltanian, M.A. Amooie, Convective Dissolution of Carbon Dioxide in 693 Deep Saline Aquifers: Insights from Engineering a High-Pressure Porous Visual Cell, Phys. Rev. Appl. 12 694 (2019). https://doi.org/10.1103/PhysRevApplied.12.034016.
- 695 [35] G.S.H. Pau, J.B. Bell, K. Pruess, A.S. Almgren, M.J. Lijewski, K. Zhang, High-resolution simulation and characterization of density-driven flow in CO2 storage in saline aquifers, Adv. Water Resour. 33 (2010) 443–455. https://doi.org/10.1016/j.advwatres.2010.01.009.
- 698 [36] A.C. Slim, Solutal-convection regimes in a two-dimensional porous medium, J. Fluid Mech. 741 (2014) 461–491. https://doi.org/10.1017/jfm.2013.673.
- A. Taheri, E. Lindeberg, O. Torsæter, D. Wessel-Berg, Qualitative and quantitative experimental study of convective mixing process during storage of CO2 in homogeneous saline aquifers, Int. J. Greenh. Gas Control. 66 (2017) 159–176. https://doi.org/10.1016/j.ijggc.2017.08.023.
- 703 [38] R. Guo, H. Sun, Q. Zhao, Z. Li, Y. Liu, C. Chen, A Novel Experimental Study on Density-Driven Instability 704 and Convective Dissolution in Porous Media, Geophys. Res. Lett. 48 (2021). 705 https://doi.org/10.1029/2021GL095619.
- 706 [39] Y. Teng, P. Wang, Y. Liu, L. Jiang, D. Wang, A spectrophotometric method for measuring dissolved CO2 in saline water, Exp. Fluids. 59 (2018). https://doi.org/10.1007/s00348-018-2594-0.
- 708 [40] Y. Teng, P. Wang, L. Jiang, Y. Liu, Y. Wei, New spectrophotometric method for quantitative characterization

- 709 of density-driven convective instability, Polymers (Basel). 13 (2021) 1–21. 710 https://doi.org/10.3390/POLYM13040661.
- 711 [41] T. Sherman, N.B. Engdahl, G. Porta, D. Bolster, A review of spatial Markov models for predicting preasymptotic and anomalous transport in porous and fractured media, J. Contam. Hydrol. 236 (2021). https://doi.org/10.1016/j.jconhyd.2020.103734.
- 714 [42] Z. Rasheed, A. Raza, R. Gholami, M. Rabiei, A. Ismail, V. Rasouli, A numerical study to assess the effect of heterogeneity on CO2 storage potential of saline aquifers, Energy Geosci. 1 (2020) 20–27. https://doi.org/10.1016/j.engeos.2020.03.002.
- 5. Bakhshian, S.A. Hosseini, N. Shokri, Pore-scale characteristics of multiphase flow in heterogeneous porous media using the lattice Boltzmann method, Sci. Rep. 9 (2019). https://doi.org/10.1038/s41598-019-39741-x.
- H. Guo, X. Zhuang, P. Chen, N. Alajlan, T. Rabczuk, Stochastic deep collocation method based on neural architecture search and transfer learning for heterogeneous porous media, Eng. Comput. 38 (2022) 5173–5198. https://doi.org/10.1007/s00366-021-01586-2.
- 722 [45] M.R. Soltanian, M.A. Amooie, N. Gershenzon, Z. Dai, R. Ritzi, F. Xiong, D. Cole, J. Moortgat, Dissolution 723 Trapping of Carbon Dioxide in Heterogeneous Aquifers, Environ. Sci. Technol. 51 (2017) 7732–7741. 724 https://doi.org/10.1021/acs.est.7b01540.
- R. Farajzadeh, P. Ranganathan, P.L.J. Zitha, J. Bruining, R. Farajzadeh., P. Ranganathan, P.L.J. Zitha, J. Bruining, The effect of heterogeneity on the character of density-driven natural convection of CO2 overlying a brine layer, Adv. Water Resour. 34 (2011) 327–339. https://doi.org/10.1016/j.advwatres.2010.12.012.
- 728 [47] M.R. Soltanian, M.A. Amooie, Z. Dai, D. Cole, J. Moortgat, Critical Dynamics of Gravito-Convective Mixing 729 in Geological Carbon Sequestration, Sci. Rep. 6 (2016) 35921. https://doi.org/10.1038/srep35921.
- R. Mahyapour, S. Mahmoodpour, M. Singh, S. Omrani, Effect of permeability heterogeneity on the dissolution process during carbon dioxide sequestration in saline aquifers: two-and three-dimensional structures, Geomech. Geophys. Geo-Energy Geo-Resources. 8 (2022). https://doi.org/10.1007/s40948-022-00377-3.
- 734 [49] Y. Liu, C.D. Wallace, Y. Zhou, R. Ershadnia, F. Behzadi, D. Dwivedi, L. Xue, M.R. Soltanian, Influence of 735 Streambed Heterogeneity on Hyporheic Flow and Sorptive Solute Transport, Water. 12 (2020) 1547. 736 https://doi.org/10.3390/w12061547.
- 737 [50] C. Chang, Q. Zhou, T.J. Kneafsey, M. Oostrom, T.W. Wietsma, Q. Yu, Pore-scale supercritical CO2 dissolution and mass transfer under imbibition conditions, Adv. Water Resour. 92 (2016) 142–158. https://doi.org/10.1016/j.advwatres.2016.03.015.
- 740 [51] R.S. Jayne, H. Wu, R.M. Pollyea, Geologic CO2 sequestration and permeability uncertainty in a highly 741 heterogeneous reservoir, Int. J. Greenh. Gas Control. 83 (2019) 128–139. 742 https://doi.org/10.1016/j.ijggc.2019.02.001.
- 743 [52] C. Doughty, K. Pruess, Modeling Supercritical Carbon Dioxide Injection in Heterogeneous Porous Media, 744 Vadose Zo. J. 3 (2004) 837–847. https://doi.org/10.2113/3.3.837.
- 745 [53] W. Amarasinghe, I. Fjelde, J.Å. Rydland, Y. Guo, Effects of permeability on CO2 dissolution and convection
 746 at reservoir temperature and pressure conditions: A visualization study, Int. J. Greenh. Gas Control. 99 (2020).
 747 https://doi.org/10.1016/j.ijggc.2020.103082.
- H. Vosper, K. Kirk, C. Rochelle, D. Noy, A. Chadwick, Does numerical modelling of the onset of dissolution convection reliably reproduce this key stabilization process in CO2 Storage?, Energy Procedia. 63 (2014)
 5341–5348. https://doi.org/10.1016/j.egypro.2014.11.566.
- 751 [55] Y.Y. Wang, X.G. Wang, R.C. Dong, W.C. Teng, S.Y. Zhan, G.Y. Zeng, C.Q. Jia, Reservoir heterogeneity controls of CO2-EOR and storage potentials in residual oil zones: Insights from numerical simulations, Pet. Sci. (2023). https://doi.org/10.1016/j.petsci.2023.03.023.
- 754 [56] R. Ershadnia, S. Hajirezaie, A. Amooie, C.D. Wallace, N.I. Gershenzon, S.A. Hosseini, D.M. Sturmer, R.W. Ritzi, M.R. Soltanian, CO2 geological sequestration in multiscale heterogeneous aquifers: Effects of heterogeneity, connectivity, impurity, and hysteresis, Adv. Water Resour. 151 (2021). https://doi.org/10.1016/j.advwatres.2021.103895.
- 758 [57] J.P. Ennis-King, L. Paterson, Role of Convective Mixing in the Long-Term Storage of Carbon Dioxide in 759 Deep Saline Formations, Proc. - SPE Annu. Tech. Conf. Exhib. 10 (2003) 2521–2532. 760 https://doi.org/10.2118/84344-ms.
- 761 [58] F. Graf, E. Meiburg, C. Härtel, Density-driven instabilities of miscible fluids in a Hele-Shaw cell: Linear

- 762 stability analysis of the three-dimensional Stokes equations, J. Fluid Mech. 451 (2002) 261–282. 763 https://doi.org/10.1017/s0022112001006516.
- E.J. Kutsienyo, M.S. Appold, M.D. White, W. Ampomah, Numerical modeling of CO2 sequestration within a five-spot well pattern in the morrow B sandstone of the farnsworth hydrocarbon field: Comparison of the toughreact, stomp-eor, and gem simulators, Energies. 14 (2021). https://doi.org/10.3390/en14175337.
- R.L. Detwiler, S.E. Pringle, R.J. Glass, Measurement of fracture aperture fields using transmitted light: An evaluation of measurement errors and their influence on simulations of flow and transport through a single fracture, Water Resour. Res. 35 (1999) 2605–2617. https://doi.org/10.1029/1999WR900164.
- 770 [61] W. M.D., W. D.J., B. D.H., W. S.K., M. B.P, Z. Z.F., STOMP Subsurface Transport Over Multiple Phases, 2012. https://stomp-userguide.pnnl.gov/documentation/guides/PNNL-21268.pdf.
- T.J. Kneafsey, K. Pruess, Laboratory flow experiments for visualizing carbon dioxide-induced, density-driven brine convection, Transp. Porous Media. 82 (2010) 123–139. https://doi.org/10.1007/s11242-009-9482-2.
- 774 [63] L. Paterson, Fingering with miscible fluids in a Hele Shaw cell, Phys. Fluids. 28 (1985) 26–30. 775 https://doi.org/10.1063/1.865195.
- J.A. Letelier, N. Mujica, J.H. Ortega, Perturbative corrections for the scaling of heat transport in a Hele-Shaw geometry and its application to geological vertical fractures, J. Fluid Mech. 864 (2019) 746–767. https://doi.org/10.1017/jfm.2019.3.
- 779 [65] H.N. Ulloa, J.A. Letelier, Energetics and mixing of thermally driven flows in Hele-Shaw cells, J. Fluid Mech. 930 (2022). https://doi.org/10.1017/jfm.2021.897.
- 781 [66] J.D. Ingle, Jr, S.R. Crouch, Spectrochemical Analysis, 1988. https://www.osti.gov/biblio/5298199.
- 782 [67] A. Riaz, M. Hesse, H.A. Tchelepi, F.M. Orr, Onset of convection in a gravitationally unstable diffusive 783 layer porous media, Mech. boundary in J. Fluid 548 (2006)87–111. https://doi.org/10.1017/S0022112005007494. 784
- 785 [68] A. Taheri, O. Torsæter, E. Lindeberg, N.J. Hadia, D. Wessel-Berg, Effect of Convective Mixing Process on 786 Storage of CO2 in Saline Aquifers with Layered Permeability, Adv. Chem. Res. 3 (2021). 787 https://doi.org/10.21926/acr.2101012.
- 788 [69] Y. Teng, P. Wang, L. Jiang, Y. Liu, Y. Song, Y. Wei, An experimental study of density-driven convection of fluid pairs with viscosity contrast in porous media, Int. J. Heat Mass Transf. 152 (2020). https://doi.org/10.1016/j.ijheatmasstransfer.2020.119514.
- 791 [70] C.P. Green, J. Ennis-King, Steady dissolution rate due to convective mixing in anisotropic porous media, Adv. Water Resour. 73 (2014) 65–73. https://doi.org/10.1016/j.advwatres.2014.07.002.
- 793 [71] C. Thomas, L. Lemaigre, A. Zalts, A. D'Onofrio, A. De Wit, Experimental study of CO2 convective dissolution: The effect of color indicators, Int. J. Greenh. Gas Control. 42 (2015) 525–533. https://doi.org/10.1016/j.ijggc.2015.09.002.
- 796 [72] R. Farajzadeh, B. Meulenbroek, D. Daniel, A. Riaz, J. Bruining, An empirical theory for gravitationally unstable flow in porous media, Comput. Geosci. 17 (2013) 515–527. https://doi.org/10.1007/s10596-012-9336-9.
- 799 [73] C.P. Green, J. Ennis-King, Steady flux regime during convective mixing in three-dimensional heterogeneous porous media, Fluids. 3 (2018). https://doi.org/10.3390/fluids3030058.

801 802